Deep tissue penetration of bottle-brush polymers via cell capture evasion and fast diffusion

Jean-Michel Rabanel [†, ‡, #, ¶], *Marziye Mirbagheri* [‡, ¶], *Mateusz Olszewski* [⁑], *Guojun Xie* [⁑], *Marine Le Goas* [‡], *Pierre-Luc Latreille* [‡], *Hermine Counil* [†], *Vincent Hervé* [†], *Rummenigge Oliveira Silva* [†], *Charlotte Zaouter* [†], *Vahid Adibnia* [‡, ⁂, *], *Mariana Acevedo* [‡], *Marc J. Servant* [‡], *Vincent A. Martinez* [§], *Shunmoogum A. Patten* [†], *Krzysztof Matyjaszewski* [⁑, #], *Charles Ramassamy* [†, #], *Xavier Banquy* [‡, #]

Affiliations

[†] INRS Centre Armand-Frappier Santé Biotechnologie, 531, boul. des Prairies, Laval, QC, CAN H7V 1B7

[‡] Faculté de pharmacie, Université de Montréal, C.P. 6128, Succursale Centre-ville, Montréal, QC, CAN H3C 3J7

[⁑] Department of Chemistry, Carnegie Mellon University, 4400 Fifth Avenue, Pittsburgh, PA, USA 15213 - 3815

[⁂] Department of applied Oral Sciences and [*] School of Biomedical Engineering, Dalhousie University, 5981, University Avenue, Halifax, NS, CAN B3H 4R2

[§] School of Physics and Astronomy, University of Edinburgh, King's Buildings, Peter Guthrie Tait Road, Edinburgh, UK EH9 3FD

[¶] These authors contributed equally to this work

[#] Corresponding authors: Jean-Michel Rabanel jean-michel.rabanel@umontreal.ca Xavier Banquy, xavier.banquy@umontreal.ca Charles Ramassamy, charles.ramassamy@inrs.ca Krzysztof Matyjaszewski, km3b@andrew.cmu.edu

Graphical table of content

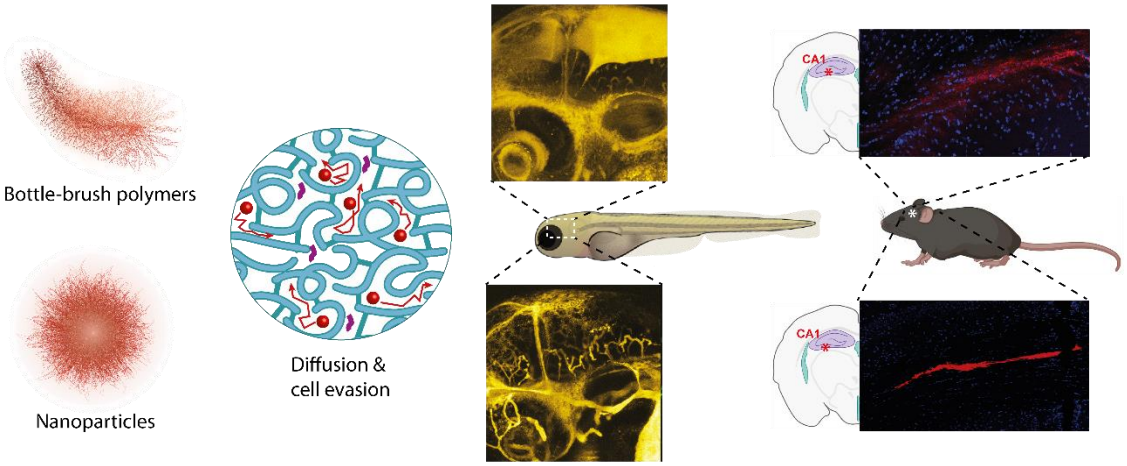

Abstract

Drug nanocarriers (NCs) capable of crossing the vascular endothelium and to deeply penetrate into dense tissues of the CNS could potentially transform the management of neurological diseases. In the present study, we investigated the interaction of bottle-brush (BB) polymers with different biological barriers *in vitro* and *in vivo* and compared it to nanospheres of similar composition. *In vitro* internalization and permeability assays revealed that BB polymers are not internalized by brain-associated cell lines and translocate much faster across a blood-brain barrier model compared to nanospheres of similar hydrodynamic diameter. These observations performed under static, no-flow conditions, were complemented by dynamic assays performed in microvessels arrays on chip and confirmed that BB polymers can escape the vasculature compartment via a paracellular route. BB polymers injected in mice and zebrafish larvae exhibit higher penetration in brain tissues, and faster extravasation of microvessels located in the brain compared to nanospheres of similar sizes. The superior diffusivity of BBs in extracellular matrix-like gels combined to their ability to efficiently cross endothelial barriers via a paracellular route position them as promising drug carriers to translocate across the blood-brain barrier and penetrate dense tissue such as the brain, two unmet challenges and ultimate frontiers in nanomedicine.

Keywords

bottle-brush polymer; blood-brain barrier; vessel-on-a-chip; zebrafish; mouse

Introduction

The field of nanomedicine has thrived on the foundations of very few paradigms. One essential paradigm is the concept of "magic bullet", the capacity of nanomedicines to modify, if not control at will, drug biodistribution. Such control should allow concentrating a drug where it is most needed in order to treat affected tissues without damaging the healthy surrounding cells. Control of biodistribution also impacts the drug's residence time in the blood stream and, therefore, its therapeutic index and efficacy. After several decades of development and hundreds of clinical trials, nanomedicines have struggled to reach the market, questioning the very foundations of their design principles. [1-3] Recent reports have shattered the paradigm of drug targeting used by many ligand-decorated nanocarriers (NCs) by suggesting that only a small fraction of drug accumulates in targeted tissues, which most of the time equals the accumulated amount obtained in untargeted systems. [2, 4-6] This debate urges scientist to rethink their methodological approach to design drug delivery systems, starting not necessarily from the drug itself but rather from the NC and optimizing its capacity to better navigate inside living organisms. [7] NCs capable of deep penetration into tissues are scarce or even inexistent. Spherical nanoparticle-based systems for example cannot diffuse freely across biological barriers such as the blood-brain barrier and in dense tissues (muscle fibers or brain tissue). This could be problematic when the objective of the formulation is to reach deep regions of the body but could be advantageous to create a localized depot that would release slowly its payload. Particles free-diffusion in dense tissues can only be achieved with particles smaller than 50 nm, which is smaller than most particle-based drug delivery systems. [8, 9] There is therefore a very strong technological need to design NCs that could replace nanoparticles and achieve deep tissue

penetration without being hindered by diffusion or cell capture. In very recent years, molecular brushes, also known as bottlebrush polymers (BB polymers), [10, 11] have emerged as a different class of drug delivery system. BB polymers have been tested in multiple biomedical applications, from drug delivery systems [12, 13] to functional coatings, [14] and lubricants for joints. [15]

BB polymers have been shown to control the pharmacokinetic (PK) of their cargo in a similar way to other drug delivery systems [16] to penetrate deeply into tumor spheroids *in vitro*. [17-20] It had been shown with cylindrical polymer brushes of different lengths (varying from 34 to 119 nm), that longer brushes displayed higher cellular uptake, lower tissue permeability, shorter blood circulation time, lower tumor accumulation and faster clearance than their shorter counterparts. [21] The extent and depth of tumor spheroid penetration of rigid Tobacco virus-like particles decreased with increasing the aspect ratio (AR) of the viral particles. [17, 22] Similar results were obtained with rod-like micelles (12 nm in width and 80 to 200 nm in length). [20] The effect of the AR was also demonstrated with poly(2-ethyl-2-oxazoline) (PEtOx)-based BBs. Increasing either the backbone or side-chain length of PEtOx BBs decreased cell uptake *in vitro* and induced an increase of circulation time in mouse blood stream. [23] Stiffer BB polymers were found to be eliminated faster from the blood stream compared to more flexible BB polymers. [16, 19, 24] Regarding organs biodistribution, increasing AR of BB polymers lead to higher uptake in organs such as liver and spleen. [16,25, 26] While the vast majority of studies involving BB polymer scrutinized their penetration capacity in tumor, this work was aimed at evaluating the capacity of these materials to penetrate dense tissues such as the brain and to translocate across the blood-brain barrier (BBB), an unmet challenge in nanomedicine.

Results and discussion

Nanoparticles and Bootle-brush polymers characterizations

The chemical structures of the BB polymers as well as the diblock copolymer used to produce the spherical NPs and their morphology are shown in Figure 1. Physical chemical properties such as size, zeta potential, grafting densities are summarized in Table 1. NPs were prepared by nanoprecipitation using PEG-*g*-PLA diblock polymers obtained by ring opening polymerization from mPEG 2kD and mPEG 5kD chain macro-initiators. [27] NPs are core-shell spheres with a hydrophobic PLA core and a shell of PEG chains at their surfaces (Figure 1A, C). TEM images obtained by negative staining at room temperature clearly showed smooth hard spheres (Figure 1C). Moreover, the glass transition temperatures of the diblock polymers are all above 40º C which is higher than *in vitro* and *in vivo* experiment temperature supporting the fact that these NPs have a hard rather than soft core. [28]

On the other hand, AFM imaging of the BB polymers (Figure 1D-F) confirmed the worm-like shape of the BB polymers on a mica surfaces. This worm-like morphology is the result of the BB polymer backbone and side-chains spreading on mica surfaces (Figure 1D-F) which is most perceptible with the Long BB polymer (Fig 1F). All the BB polymers have the same grafting density of side chains (n+m)/(n+m+p) of approximately 50%, (see table 1) and degree of polymerization (DP = 53-57). At such low grafting density and small side chain length, the BB macromolecules are able to coil and behave as flexible worm-like) chains rather than rigid rods. [29, 30]

Distributions of BB polymers contour length obtained from AFM are available in SI (Figure S2). [28, 31]

BB polymer cross-section was obtained from AFM images and was found to vary between 24.5 and 27.8 nm (Table 1). These values are in good agreement with theoretical calculation based on the DP of side chain (DP = 52-57) with a repeat unit size of 0.25 nm. The aspect ratio (AR), of the different polymers was found to vary between 2.9 to 6.7 (Table 1). The size range of the NPs and BB polymers is representative of most nanoscale drug delivery carriers, with size in the 50 to 150 nm bracket.

To enable tracking and quantification, NPs and the BB polymers were tagged with a Cy5 fluorescent probe. The amount of fluorescent probe on each object was quantified as the amount of fluorescence intensity by mass of material. NPs as well as Short and Long BB polymers have similar level of fluorescence per mass of material, only Medium BB polymers exhibited significantly less amount (Figure S3).

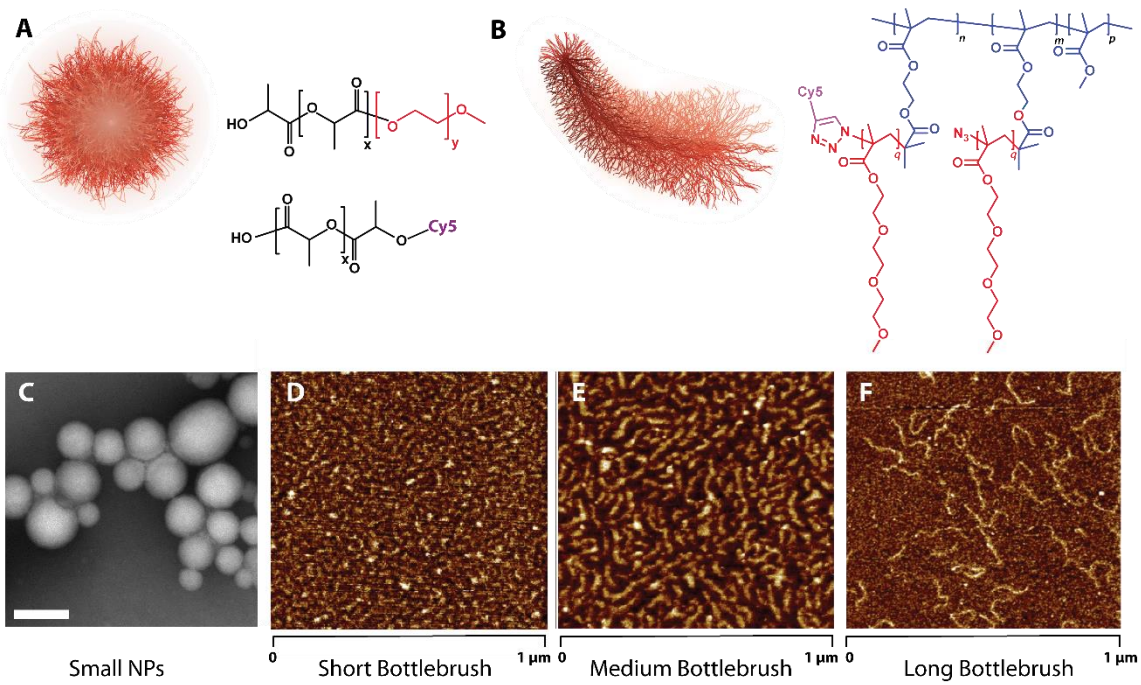

Figure 1. Nanoparticles and Bottle-brush polymers chemical structure and morphology. (A) Schematic representation of a NP and chemical structure of the diblock polymer (and fluorescent polymer) used to produce it (x=275; y=45 or 114); **(B)** Schematic representation of a BB polymer chain with its chemical structure (see Table 1 for n, m, p and q values)**; (C)** TEM image of NPs (scale bar: 50 nm); AFM topographic images acquired in air of **(D)** Short, **(E)** Medium, and **(F)** Long BB polymers.

Table 1. Nanoparticles and Bottle-brush polymers physical properties.

	Diameter (DDM)		Zeta potential		Cross-section length *		BB Contour length *		Aspect ratio	BB Backbone size	Side chains per BB molecule		PEG grafting density		PEG
	nm		*mV*		*nm*		*nm*						NP	BB	DP
	Z-avg	Đ	ζ	SD	*T*	*SD*	*L*	SD		*n+m+p*	*n+m*	*q*	*chain/nm²*	chain/nm	
Small NPs	61.5	0.04	-5.1	8.1	NA		NA		1	NA	NA	NA	0.33	NA	114
Large NPs	93.1	0.12	-6.2	9.1	NA		NA		1	NA	NA	NA	0.2	NA	45
Short BB	88.0	0.34	-4.2	5.8	25.9	4.8	76	16	2.9	209	115	53	NA	1.51	NA
Medium BB	124.7	0.33	-1.7	6.2	27.3	4.4	101	25	3.7	487	275	54	NA	2.72	NA
Long BB	164.3	0.31	-4.2	5.1	24.3	3.6	163	39	6.7	829	459	57	NA	2.82	NA

Abbreviations

SD	Standard deviation
Đ	Dispersity
DP	Degree of polymerization
q	Number of monomer units in side chains
n	Number of side chains per BB polymer molecule carrying a Cy5 moiety
m	Number of side chains per BB polymer molecule not carrying a Cy5 moiety
p	Number of spacer monomer in the backbone
*	Determined from AFM images

Cytotoxicity & Endocytosis assays

Cytotoxicity of NPs and BB polymers was evaluated on three different murine cells lines, *i.e.* bEnd.3, a vascular endothelial cell from mouse brain; [32] N2a, a neuronal (neuroblastoma) cell line; [33] and N11, a brain microglia cell line. [34] No effect on the cell proliferation (Resazurin test) and membrane damage (LDH release test) were observed at the maximal concentration used in all cell culture assays (Figure S4).

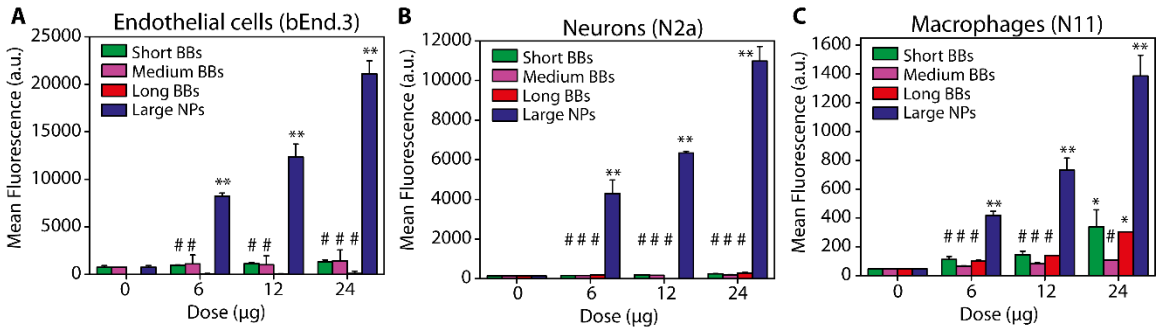

Figure 2. Bottlebrush polymers exhibit slower internalization rates compared to nanoparticles. FACS analysis of the internalisation signal from endothelial (A), neuronal (B) and microglia (C) cell lines after 24-hour exposure to three different doses of NPs or BB polymers. ** $p<0.01$, * $p<0.05$, # Not significantly different from control

The internalization of BB polymers obtained by flow cytometry in all the cell lines at either 4-h (Figure S5) or 24-h (Figure 2A & 2B) was far smaller than NPs, irrespective of their size. On the other hand, NPs uptake was clearly detected and increased significantly between 4-h (Figure S5) and 24-h of incubation (Figure 2A). These measurements were performed after several rounds of PBS washing to ensure that the measured fluorescence intensity correspond to the intracellular nanomaterials. Moreover, examination of cells by fluorescence microscopy did not reveal any fluorescent signal associated to the cellular membrane, confirming that the detected signal in flow cytometry was from the internalized nanomaterials only.

Calculations of the different doses expressed as the number of particles or macromolecules show that BB polymer lowest concentration (6µg/well) was still five times higher than the highest NPs concentration tested (24µg/well). Still, no evidence of internalisation of the BB polymer were observed either by flow cytometry (no significant difference between BB polymer internalisation and cell control, Figure 2 and Figure S5) or by confocal microscopy (Figure 3C).

As in the case of N11 cell line, BB polymers uptake was insignificant compared to non-exposed cell control at 4 hours (Figure S5). However, at 24 hours, a slight increase in fluorescence signal was recorded for Short and Long BBs (Figure 2C). The lower signal observed for the Medium BBs was likely due to its lower intrinsic fluorescence (Figure S3). Therefore, N11 cells, considered as brain resident macrophages, have the ability to capture BB polymers more efficiently, most probably via phagocytosis. [34] PEGylated NPs are mainly internalized by macropinocytosis in bEnd.3 cells, a rather non-specific internalisation process. [27] Regarding the BB polymer, considering the low level (or near absence) of internalisation such a study was not deemed possible to conduct.

In summary, except for macrophage-like cells, BB polymers are not significantly endocytosed by cells found in the brain microenvironment. On the other hand, NPs with comparable hydrodynamic diameters showed higher internalization in all cell lines. Similar observations have been reported for PEGylated nanofibers exhibiting a crystalline core, [35] for short rod-like micelles [18] and for a PEGylated tobacco mosaic virus. [17, 22] These results, along with our observations, tend to suggest that particle AR plays an important role in the uptake mechanism of these nano-objects and confirm that elongated nanoparticles can evade capture by cells more efficiently than spherical ones.

In vitro cell barrier translocation assays

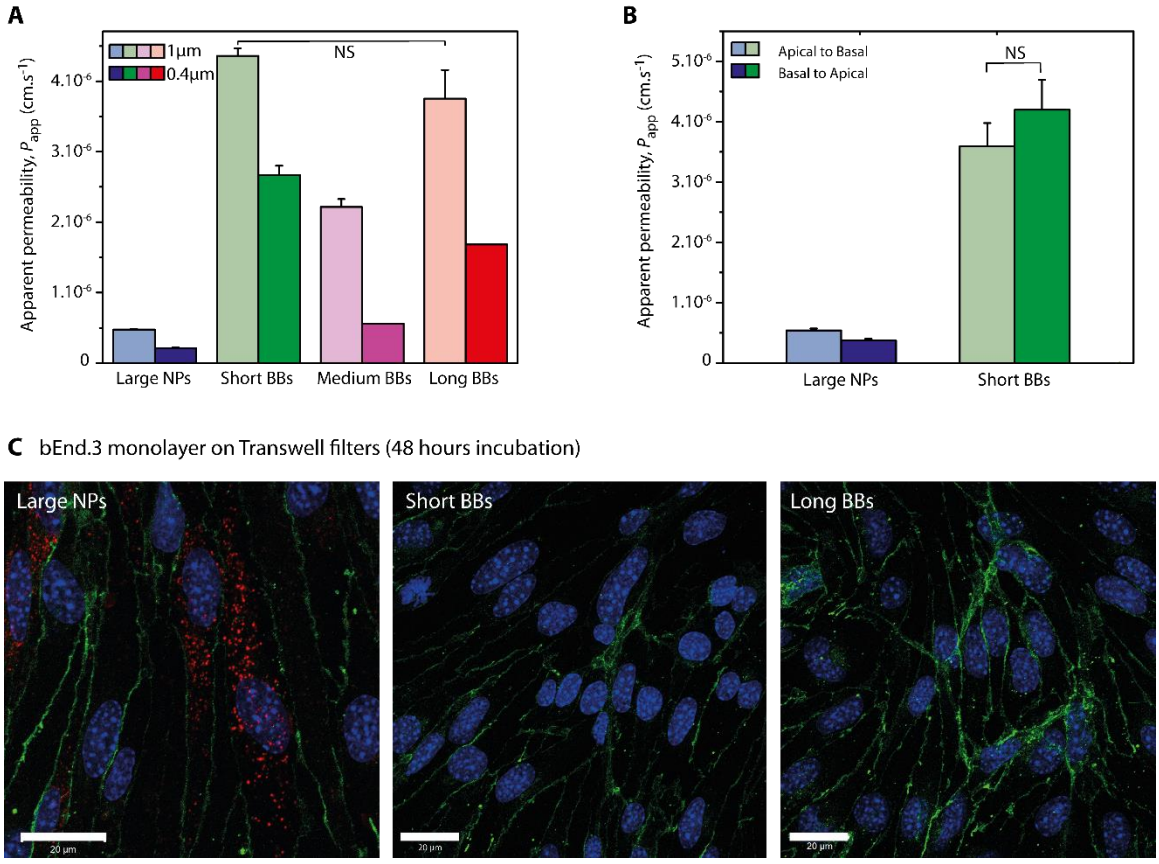

Figure 3. Bottlebrush polymers translocation is faster than nanoparticles (A) Apparent permeability, *Papp*, of NPs vs BB polymers using insert filters of different pore size (1µm vs 0.4µm) after 24-hour incubation; **(B)** Comparison of *Papp* values between Apical to Basal and Basal to Apical transport directions (1µm pore transwell); **(C)** Confocal images of the cell monolayer integrity (bEnd.3 cells) after transcytosis experiments (24-hour incubation). Staining: Blue (Hoe 33342): cell nucleus, Red: NPs or BB polymer; Green: tight junctions (Claudin-5 immunodetection). Scale bar: 20µm.

NPs and BB polymers translocation across cell monolayers mimicking the BBB was quantified in a transwell assay. Apparent permeability (P_{app}) and cell imaging were performed to compare both types of materials. P_{app} of the Short BB polymer was eight to ten times higher compared to PEGylated NPs of comparable hydrodynamic size (Figure 3A).

The pore size of the insert membrane used for the assay (1 µm vs 0.4 µm) had a significant impact on the values of P_{app} indistinctly of the nature of the material tested. The values of P_{app} decreased systematically by a factor of two when reducing the pore size by almost the same factor, suggesting a diffusion-limited translocation mechanism rather than active translocation (Figure 3A).

The measured values of P_{app} of the BB polymers at 24 and 48 hours did not present any clear dependence on the polymer size, although the values at 48h were significantly smaller compared to 24h, suggesting that equilibration was nearly achieved (data not shown).

P_{app} values were also found identical in apical-to-basal and basal-to-apical transport directions (Figure 3B). This observation is an indirect confirmation that no convective or active transport was involved in BB polymers and NPs translocation through the cell monolayer. Post-assay imaging of the bEnd.3 cell monolayer on the inserts' membrane showed intact tight junctions for both BB polymers and NPs treatments. Imaging of the cell monolayer after the translocation assay did not reveal the presence of BBs macromolecules inside or associated to the cells' membrane, while NPs were clearly seen in vesicular organelles inside the cells (Figure 3C). This is consistent with the uptake experiments conducted on non-porous substrate showing low levels of internalization in bEnd.3 cells for the BB polymers compared to NPs (Figure 2A).

The collection of evidence described so far suggests that BB polymers, unlike NPs, translocate through cell monolayers via the paracellular route. On the other hand, imaging of the cell monolayer did not show any signs of alteration of the tight junctions after

incubation with either BB polymers or NPs, which confirmed that exposure to the BB polymers or the NPs did not create any induced porosity in the cellular monolayer.

In addition, we noticed that lowering the incubation temperature to 4ºC decreased the translocation of BB polymers by a factor of 2.20-2.34 (Figure S6). If the translocation of the BB polymers was controlled by the diffusion of the polymers through the cells, the value of P_{app} should be dominated by the diffusion coefficient of the polymer in the cell compartment. Diffusion coefficient is proportional to thermal energy (KT) and depends on the medium viscosity η as described in the Stokes-Einstein equation (Eq. 2). Considering the viscosity of water at 4 and 37ºC, the ratio of the diffusion coefficients at 37ºC and 4ºC, is 2.5. Therefore, the decrease in P_{app} induced by lowering the temperature correlates directly with the decrease in diffusion coefficient (Figure S6). This observation suggests that BB polymers translocation through the cell monolayer is not controlled by diffusion through the cells (transcellular route) but rather by diffusion in between cells (paracellular route). Indeed, in the paracellular route, diffusive transport is controlled by the dimensions of the constrictions in between cells and the diffusion coefficient. Conversely, translocation route of PEGylated NPs is transcellular rather than paracellular, and is strongly size-dependent as previously shown. [27] BB polymers and NPs translocation mechanisms appear to be quite different even at comparable hydrodynamic size. In the case of BB polymers, hydrodynamic size has little to no impact on the value of P_{app} and therefore translocation capacity, which is consistent with a mechanism involving BB crawling in between cell walls to achieve translocation.

According to AFM images (Figure 1), BB polymers demonstrate the ability to bend and curve, suggesting a high flexibility. Ribovski *et al.* recently reported that hard nanogels

experienced higher cellular uptake compared to soft nanogels while higher rates of transcytosis were observed for soft nanogels. [36] The authors suggested that differences in stiffness are directly linked to differences in endocytosis/uptake pathways and can lead to an enhancement of intracellular trafficking toward exocytosis of soft nanomaterials (from the opposite face of the cell monolayer). However, in the context of the present study, intracellular transport of BB polymers is discarded since endocytosis results and confocal imaging led to the conclusion of a paracellular translocation route. Therefore, it seems that particle shape rather than flexibility is at the origin of the differences in translocation routes.

Escape of NPs and BB polymers from the vasculature

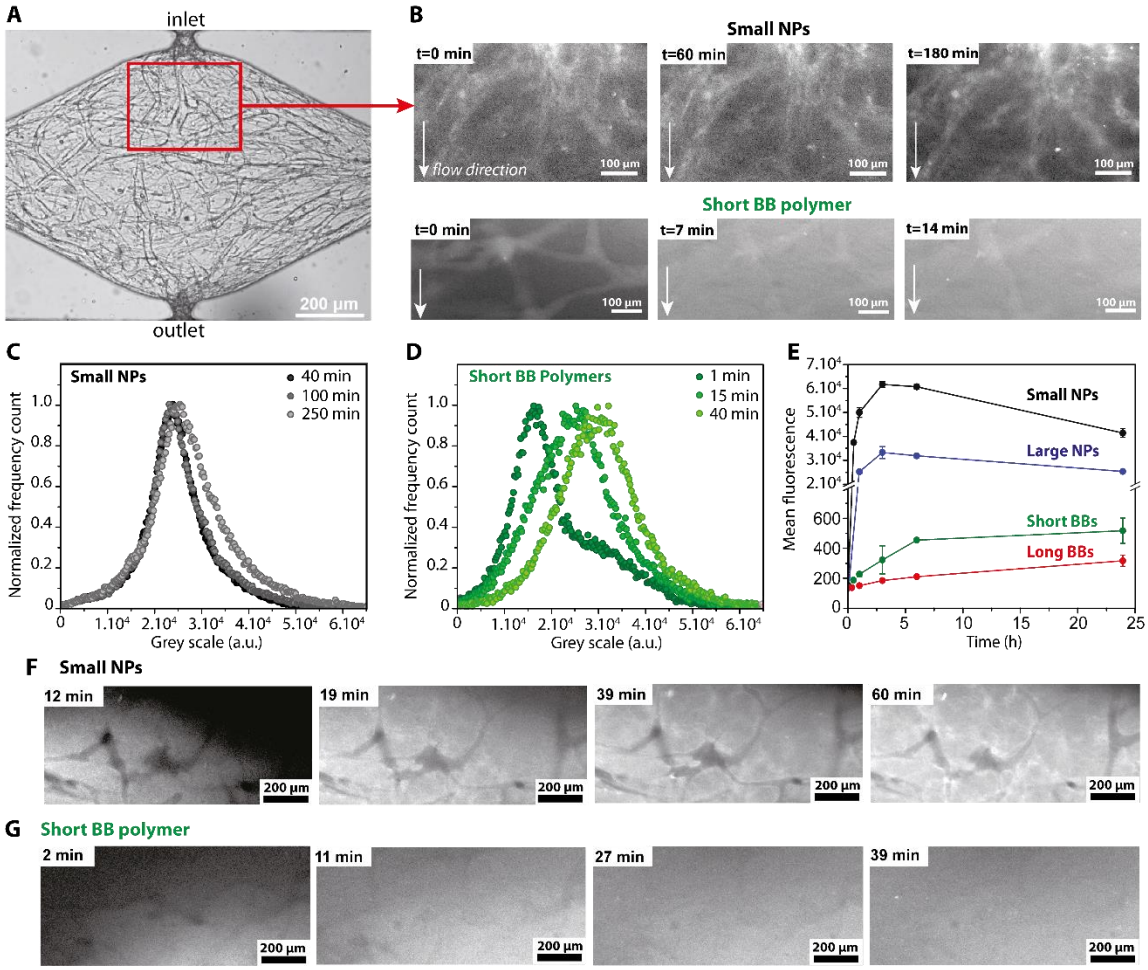

Figure 4. Bottlebrush polymers extravasate from microvessels faster than nanoparticles. (A) Image of the diamond-shape microchamber used to grow the perfusable microvessel network. **(B)** Time lapse imaging of Small NPs (panel B, top) and Short BB polymers (panel B, bottom) extravasation from the microvessels to the ECM. Arrow indicates the flow direction. Time evolution of the normalized frequency count of the grey values in the brightfield images of the diffusion time-lapse (panel B) are shown in panel **(C)** for Small NPs and **(D)** for Short BB polymers**. (E)** Uptake kinetics of NPs (Large NPs: Blue; Small NPs: Black) and BB polymers (Short BBs: Green; Long BBs: red) in endothelial cells (HUVECs), n = 3 per time point. Time lapse of Small NPs **(F)** and Short BB polymers **(G)** diffusion from the ECM into the microvessels.

To further demonstrate the ability of BB polymers to rapidly translocate through biological barriers such as the endothelium of blood vessels, we assessed the capacity of NPs and BB polymers to diffuse inside-out and outside-in a vascular network grown in a microfluidic device (Figure 4A). Fabrication and cell seeding of the microvessel-on-a-chip device are

thoroughly described in the Supporting Information file (Figure S7-S12). The vascular network was grown in a fibrin gel until maturity which was attained when a complex, yet clearly visible, interconnected network of cell-lined capillaries were formed. Using the format of a microchip to create such network of vessels allows to infuse NPs or BB polymers in a controlled manner and to image simultaneously their transport and distribution throughout the chip. When infused inside the capillaries (t = 0 min), the NPs remained confined in the vessels for several hours (Figure 4B, top), whereas the BB polymers quickly extravasated and invaded the ECM within a few minutes Figure 4B, bottom). These observations were confirmed by analyzing the intensity frequency count in the region of interest. The distribution frequency count of grey values of NP-infused vessels shifted slightly towards higher values after 40 minutes of infusion, indicating that the NPs were slowly escaping the vessels and invading the extracellular matrix space. For the BB polymers, the situation was significantly different. The frequency count distribution was displaced towards high grey values within minutes post-infusion, demonstrating the broad diffusion of the polymers throughout the whole region of interest (Figure 4 C &D).

In a second assay, we confirmed that BB polymers were able to diffuse back into the vessels when infused in the extracellular space. In this test, BB polymers or NPs were slowly infused in the ECM, and their distribution was monitored over time. For this assay, the microvessels were not connected to the chip infusion channels. The image analysis confirmed that, as opposed to BB polymers, the NPs were not able to intravasate in the vessels and to occupy the vessels inner space (Figure 4F & G).

The rapid extravasation of the BB polymers compared to NPs supports a different transport mechanism between the two materials. However, to verify that the BB polymers were not

taken up by the endothelial cells forming the vessels, a kinetic study comparing NPs and BB polymers uptake was performed over a 24-hour period (Figure 4E). The experiment results confirmed that BB polymers internalization levels were much lower than those of the NPs (ratio of about 1:100). These results support the notion that rapid diffusion of BBs out of the vessels is related to their ability to escape capture and endocytosis by vascular endothelial cells (VECs) and to their rapid diffusion in the ECM. These observations are in line with the results obtained in the Transwell assays and confirm that BB polymers are more likely to extravasate via a paracellular route while NPs of similar size mostly stay trapped in the microvessel network.

Diffusion of NPs and BB polymers in extracellular matrix emulating hydrogels

The results obtained from *vessels-on-a-chip* experiments support the idea that BB polymers can on one side extravasate rapidly from blood vessels through nanopores between cells, and on the other side diffuse much faster in dense tissues without being taken up. To better understand these significant properties, experiments aiming to characterize the diffusion ability of BB polymers were performed. BB polymers and NPs of similar size were placed in a fibrin hydrogel emulating the ECM and their dynamics was characterized using Differential Dynamic Microscopy (DDM) (Figure 5A).

The intermediate scattering functions (Figure 5B) obtained by DDM showed that diffusion was slower in the gel for all particles, compared to diffusion in water. To compare the dynamics of BB polymers and NPs, the ratio of the diffusion coefficients in the gel and in water, D_{gel}/D_{water}, was calculated for both the NPs and the BB polymers. The BB polymers presented higher ratios than the NPs of similar hydrodynamic size (Figure 5C), showing that their diffusion was faster in the gel. Between the two BB polymers, the shorter one

was found to diffuse better in the gel, even if BB polymer cross-section were the same for all of them (Figure 5C).

Our results correlate well the observations reported in the literature, where faster diffusion of elongated nano-objects was demonstrated in gels, for both rigid and soft particles. This also echoes reports of flexible filamentous viruses demonstrating their capacity to diffuse in polymer solution over an order of magnitude faster than spheres of similar sizes. [37] Furthermore, when comparing objects with similar cross sections but different lengths, a mathematical model for diffusion in a spheroid system demonstrated similar results as ours, *i.e.*, that the lower AR diffused more efficiently. [17]

Differences in diffusion mechanism may account for the difference in biodistribution between BB polymer and spherical hard polymer NPs. In a hydrogel such as the ECM, spherical NPs are expected to be trapped in the porous network when their size nears the matrix pore size, a phenomenon well described by several theoretical models.[38] BB polymers are able to diffuse through much smaller pores and adopt a diffusion mechanism described by the well-established Zimm and Rouse theories.[39, 40]

An early mechanistic study suggested flexible and long macromolecules use reptation to achieve fast diffusion in agarose gels, whereas rigid and/or spherical macromolecules remain trapped in gel pores. [41] Rotational diffusion combined with conformational adjustment were invoked to explain the superior capacity of flexible rodlike particles to diffuse, as they can bend and conform to the pores of the gel. [42] Overall, multiple diffusion modes have been suggested for elongated and/or flexible objects in confined environments: reptation [41, 43], jiggling and flying across gel pore, [42] and hopping diffusion. [44, 45] All these

modes facilitate faster diffusion of elongated nano-objects compared to spherical ones in porous matrices or crowded environments.

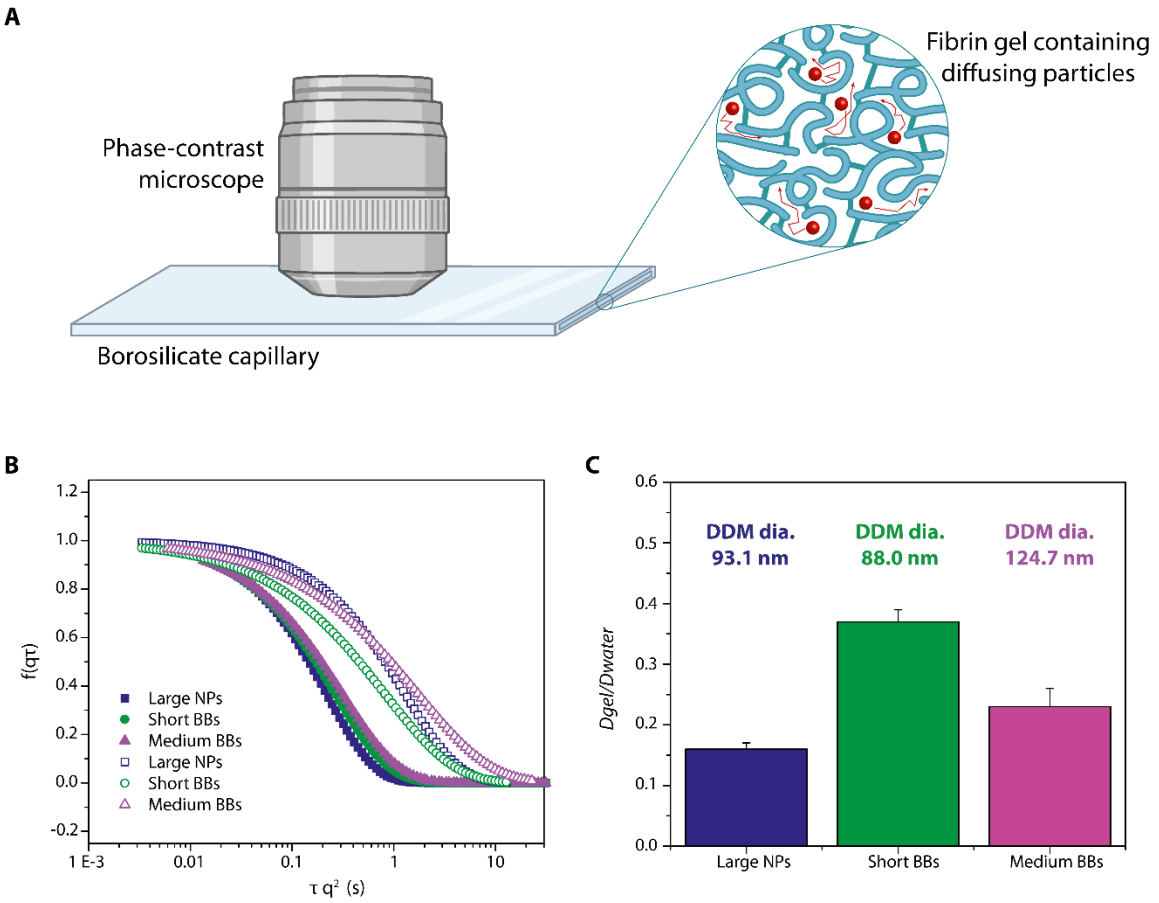

Figure 5. Measure of NPs and BBs diffusion in ECM-like gel. (A) Experimental set-up of DDM measurements; **(B)** Intermediate scattering function (ISF) of nanomaterials in water (■, solid symbols) and gel (□, open symbols); **(C)** Ratio of diffusion coefficients between gel and water (D_{gel}/D_{water}) for the Large NPs, Short and Medium BB polymers.

Nanoparticles and bottle-brush polymers biodistribution in Zebrafish larvae

Zebrafish larval model has been proposed for preclinical screening of nanomedicine toxicity [46] and to study their systemic circulation. [47] Moreover, zebrafish larvae could be a predictive model for nanomedicine circulation time in mammals [48] and organ

biodistribution. In this regard, zebrafish larvae could be considered as an *in vivo* microfluidic model able to give insights on the ability of nano-objects to remain in circulation, interact with the vascular endothelium, and eventually extravasate from the blood compartment.

To assess the biodistribution of NPs and BB polymers in the zebrafish, 48-hour post-fertilisation (hpf) zebrafish larvae were injected in the duct of Cuvier with either NPs or BB polymers. In order to evaluate the interaction of these nano-objects with the vascular endothelium and to detect any signs of extravasation, a zebrafish strain carrying the GFP-tag on endothelial cells (*Tg (flk1:EGFP)*) and a wild type (TL) strain were used. Additionally, the *Tg (vglu2a:RFP)* strain, which exhibits vesicular glutamatergic receptor tagged with Red Fluorescent Protein, were used to provide finer insights into NPs and BBs biodistribution inside the brain. [49]

In a first series of experiments, an identical weighted dose of NPs and BBs was injected in *Tg (flk1:EGFP)* zebrafish larvae by tuning the injection volumes (2-5nL/injection). At 1-hour post-injection (hpi), Large NPs remained confined in the vascular compartment (Figure 6A &D), while Long BBs quickly left the vascular compartment (Figure 6B). BB polymers were found in tissues such as the caudal venous plexus (CVP), caudal, dorsal, and ventral fins. Strikingly, BB polymers could also be found in brain ventricles, mainly in the hindbrain ventricle (IV ventricle), but in midbrain and forebrain ventricles as well (Figure 6B). The shape of the ventricles as well as the midbrain-hindbrain restriction could be clearly delineated thanks to the fluorescence signal from the BB polymers present in this organ (Figure 6B, Brain). However, the entry route of BB polymers inside cerebral ventricles is still unknown. One hypothesis could involve a passage from the blood

circulation through the choroid plexus, [50] or by diffusion across tissues and ependymal lining. BB polymers were also found around blood vessels of the otic capsule, the eyes, and the lens (Figure 6D, Brain). Some residual fluorescence was still found associated with the blood compartment: in brain microvessels (Figure 6B & D, Brain), in intersegmental trunk vessels (Figure 6D, Trunk), and in the common vein (duct of Cuvier). Fluorescence emanating from BB polymers was found only at the periphery of the fibrous notochord but not inside (Figure 6B). Above the yolk sack, an intense fluorescence signal was associated with either the pronephros or the intestinal track (Figure 6B).

Control injection of PBS revealed no background Cy5 signal in wild type (TL) larvae (Figure S13A). Control injection of pure Cy5 (free dye) lead to minor labeling of gastrointestinal track cell lining as well as skin cells (Figure S13B), demonstrating that fluorescence distribution observed upon NPs or BBs injections was unequivocally emanating from these objects and not from free dye molecules.

At 24 hpi, NPs remained largely in circulation in the vascular compartment thanks to their colloidal stability in biological medium and their inability to significantly cross vascular endothelium over this time interval. On the other hand, the biodistribution of BB polymers was very different and evolved quickly with time (Figure S14). At 24 hpi, BB polymers appeared as “sucked-out” from the whole organism and concentrated in the yolk sack. Short and Medium BB polymers biodistribution at 1 hpi and 24 hpi is very similar to the Long BB polymer biodistribution presented above (Figure S15-16) suggesting a minor role of BB length in the range tested.

This pattern of biodistribution was also observed in exquisite fine details in wild type (TL) larvae (Figure S17 & Movies of confocal imagse of larvae Head, M1 and trunk, M2 in Supporting Information). Since the BB polymers extravasate faster than NPs, we compared biodistribution patterns of BB and NPs to fluorescently labeled Dextran as control. Low molecular weight Dextran is well known to extravasate via diffusion through small pores present in blood vessels, while high molecular weight Dextran is expected to circulate in the blood stream for an extended period of time. [51] The distribution of calibrated size dextrans (10kD, 150kD, and 2MD) injected in wild type (TL) zebrafish larvae was assessed following the same protocol (Figure S18). Small 10kD Dextran at 1 hpi displayed a prominent location in fins, cerebral ventricles, around otic capsule and eyes. This distribution pattern was not altered at 24 hpi. Medium size 150kD Dextran was found at 1 hpi in the arterial and venous system in the caudal region (Figure S18). At 24 hpi however, Dextran was observed in the fins and to some extend in cerebral ventricles (IV). Large 2MD dextrans displayed a strong fluorescent signal in the vascular compartment but no signal could be found in fins, cerebral ventricles, and yolk sack (Figure S18) as previously demonstrated. [51]

These observations confirm that NPs exhibit a biodistribution pattern similar to large 2MDa fluorescent dextran and remain largely in the blood compartment. On the other hand, BB polymers have a biodistribution pattern very similar to small 10kD Dextran at short incubation time (1 hpi) which suggests that they escape the blood stream via blood vessels small pores. At 24 hpi, unlike 10 or 150kD dextrans, BBs appeared to be washed away from the larvae body and concentrated in the yolk sack (Figure S18). Therefore, at 24 hpi no correlation could be drawn between low molecular weight dextrans and BBs

biodistribution patterns. The reason behind the tropism towards the yolk sack is unclear, but it does not seem to depend on molecular weight nor hydrodynamic size.

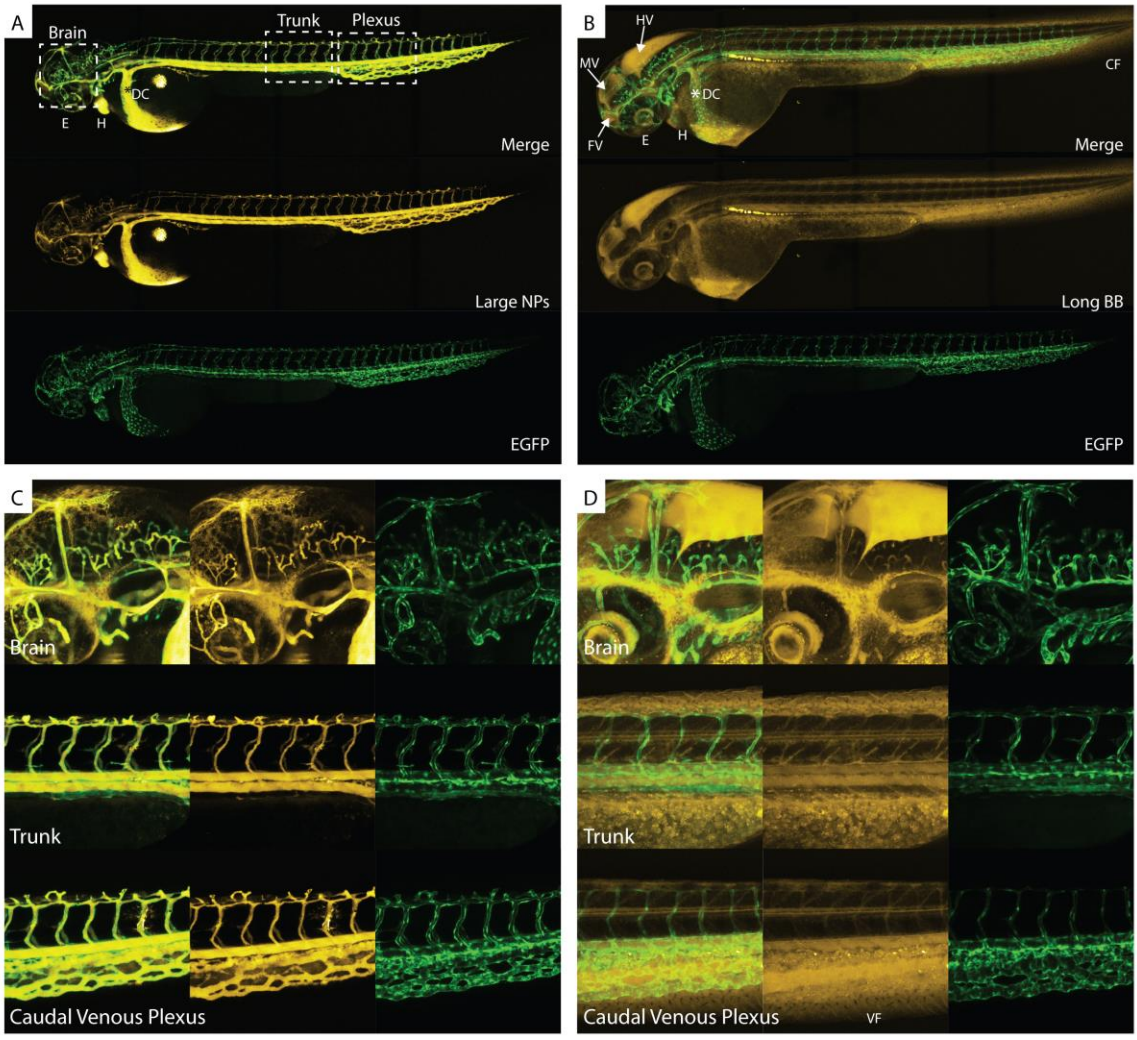

Figure 6. Bottlebrush polymers rapidly escape the blood stream and distribute broadly into tissues in the *Tg (flk1:EGFP)* zebrafish larvae. (A) Biodistribution of Large NPs, 1 hour post injection in the Duct of Cuvier; **(B)** Long BB polymers biodistribution 1 hour post injection in the Duct of Cuvier; **(C)** Brain, Trunk and Caudal Venous plexus confocal images (X20 enlargement) of Large NPs distribution; **(D)** Brain, Trunk and Caudal Venous plexus confocal images (X20 enlargement) of Long BB polymers distribution. Yellow-White channel: NPs or BB polymers; Green channel: EGFP expressed in vascular endothelial cells. Abbr. HV: Hindbrain ventricle; MV: Midbrain ventricle; FV: forebrain ventricle; E: Eyes; H: Heart; *DC: Duct of Cuvier, injection site;

The capacity of BB polymers to escape rapidly the vascular compartment is quite unusual and was observed in all the veno-arterial system and even in the brain microvasculature. Interestingly, the escape of BB polymers from the brain vasculature and diffusion into the cerebral tissue did not translate into the colocalization of the polymers with glutamatergic neurons. When zebrafish *Tg (vglu2a:RFP)* larvae were used (Figure S19) no significant colocalization signal of NPs or BB polymers with glutamatergic neurons in the brain (Figure S20) could be quantified. This observation is in line with previous *in vitro* experiments showing minimal BB polymers uptake from mouse neuronal cells (Figure 2 and S5). These experiments suggest that, in the case of BB polymers, extravasation from the blood compartment does not necessarily translate into a higher uptake by cerebral tissue cells but rather into a broad distribution.

When analyzing the colocalization signal between GFP from the VEC and Cy5 from NPs or BB polymers, a significant fraction of NPs appeared to be endocytosed (or strongly associated) with VECs in the brain, trunk, and CVP as early as 1 hpi (Figure 7A, D & G). At 24 hpi, NPs signal in the CVP was divided between blood-circulating NPs (white signal in the lumen of main vessels), NPs colocalized with VECs (red signal), and immobile NPs, that were either taken up by macrophages or adhering to the vascular endothelium (white signal in Figure 7H). On the other hand, BB polymers' colocalization signal showed very weak association to VECs even at 24 hpi in the head and trunk area (Figure 7A & D). In the CVP however, BBs had almost completely disappeared from the blood circulation and fins, but the remaining BB polymers were strongly colocalized with VECs (Figure 7G & I). The residual quantity (non-colocalized) is associated with resident macrophages or

simply adhering to the surface of the vessels, as seen in colocalization images (Figure 7I). These results correlated well with *in vitro* endocytosis and transcytosis assays where a poor uptake of BB polymers was observed. These results also suggest that BB polymers extravasation does not involve a transcellular pathway *in vivo*, as was determined from *in vitro* experiments. It can be concluded that BB polymers have the ability to extravasate vessels by crossing intercellular junctions as observed *in vitro.* Moreover, the comparison with molecular weight markers shows that the biodistribution pattern (spatially and temporally) it is not strictly an effect based on size.

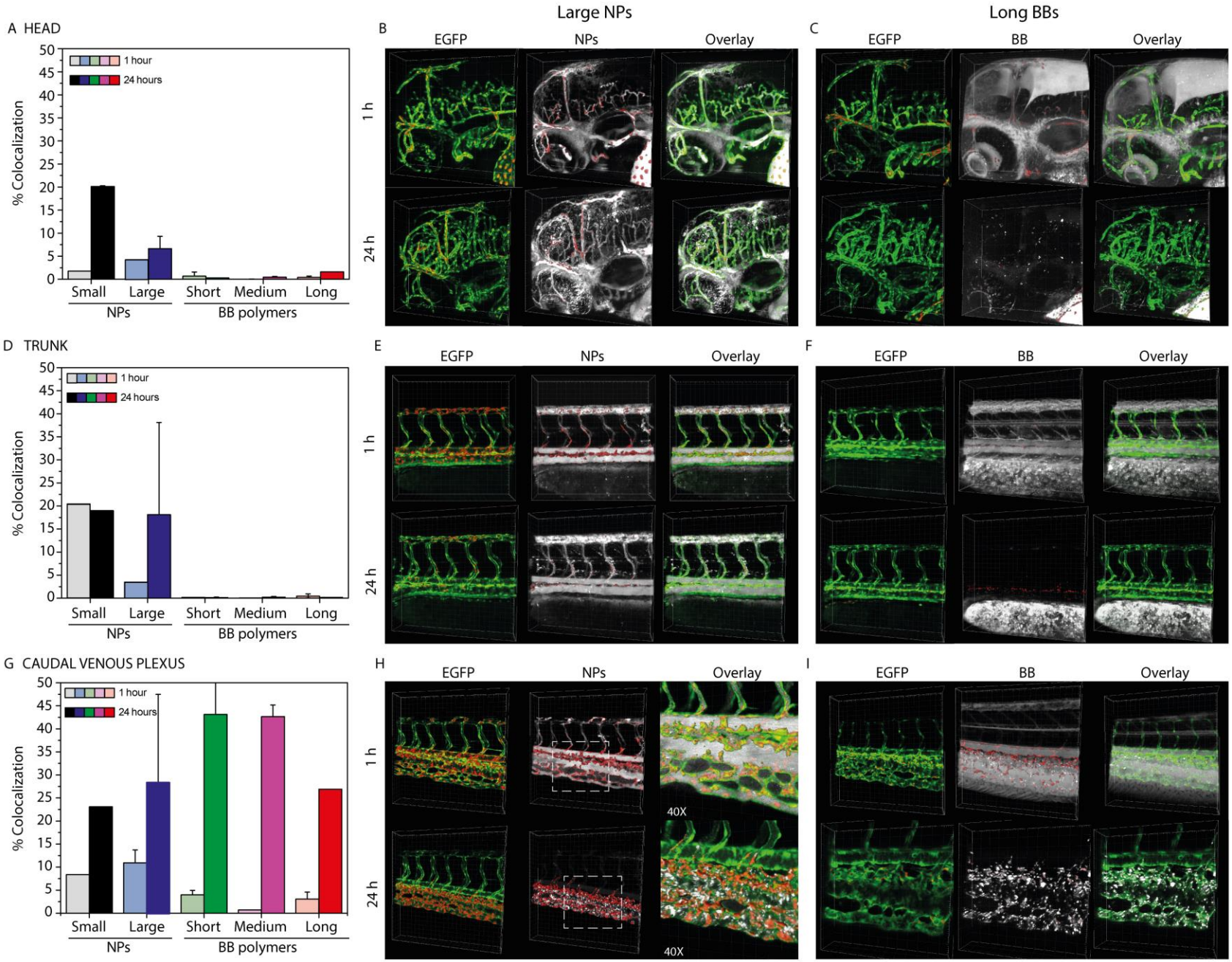
A HEAD
% Colocalization
1 hour
24 hours
Small
Large
Short
Medium
Long
NPs
BB polymers
B
Large NPs
EGFP
NPs
Overlay
1 h
24 h
C
Long BBs
EGFP
BB
Overlay
D TRUNK
E
F
G CAUDAL VENOUS PLEXUS
H
I
40X

1

Figure 7. Bottlebrush polymers are not captured by vascular endothelial cells. Colocalization analysis of NPs and BB polymers with EGFP expressed in endothelial cells' cytosol. Green channel: EGFP expressed in the cytoplasm of vascular endothelial cells; White channel: NPs or BB polymers; Red channel: Colocalization of green and white voxels as determined with Imaris® 9.2. (A to C) Colocalization of NPs or BB polymers and endothelial cells voxels in the brain vasculature at 1 and 24h post-injection; (D to F) Colocalization of NPs or BB polymers and endothelial cells voxels in the trunk vasculature at 1 and 24h post-injection; and (G to I) Colocalization of NPs or BB polymers and endothelial cells voxels in the caudal venous plexus vasculature at 1 and 24h post-injection. (n=2 to 5)

Distribution in mouse cerebral tissue

Direct injection of therapeutic agents into the cerebrospinal fluid (CSF) has been considered as a promising administration route to avoid crossing the BBB and to reach the cerebral tissue. It had been argued that therapeutics can diffuse from the CSF through the ependymal cell lining to reach the brain parenchyma [52] or alternatively, to penetrate along the arterial blood vessels perivascular space. [53] However, both therapeutic routes are highly disputed. The diffusion of large entities from the CSF into the brain parenchyma has been questioned, [54] while the extent of glymphatic/perivascular flow is still unclear. [55]

To test the viability of such administration route with nanometric transporters such as NPs and BB polymers, two types of intracerebral administration by-passing the BBB were tested: an intracerebral ventricle injection (ICV) to investigate the ability of NPs and BB polymers to diffuse into the brain from the CSF; and an intra-hippocampal injection (IHI) to assess the diffusivity of NPs and BB polymers in the brain parenchyma (Figure S21).

ICV injection of NPs resulted in a large and stable deposit on the ependymal cell layer adjacent to the injection site, with a limited penetration into surrounding brain tissues along the ventricular walls (Figure S22). On the other hand, the absence of fluorescence signal at the site of injection indicated that the BB polymer was rapidly washed out and immediately diluted in the CSF and/or surrounding tissues (Figure S22). Re-entry from meningeal vessels perivascular space along penetrating arteries was not observed. Even though NPs and BB polymers exhibited very different behavior when administrated via ICV, the lack

of penetration into the cerebral tissue suggests that this route of administration does not allow to reach deep regions of the brain.

Therefore, in a second set of experiments, NPs or BB polymers were directly injected into the hippocampus (CA1 area, Figure S21). The hippocampus is a cerebral area involved in learning and memory. [56-58] Therefore, this area could be a therapeutic target to treat neurodegenerative diseases and dementia such as Alzheimer's disease. [59-64]

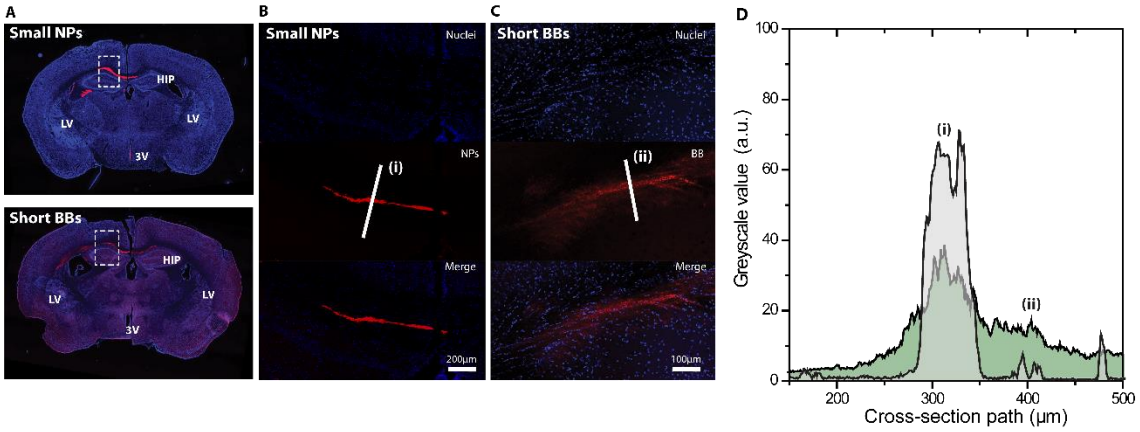

Figure 8. BB polymers diffuse deeply into the cerebral tissue after intra-hippocampal injection. **(A)** Two brain slices showing the distribution of NPs and BB polymers post intra-hippocampal injection. Blue channel: Nucleus staining; Red channel: NPs or BB polymers; Abbreviation: Lateral ventricles (LV), Dorsal 3rd ventricles (3V), hippocampus (HIP), CA1: field of the hippocampus targeted by the injection. Confocal image of the region of interest depicted in (A) after injection of Small NPs **(B)** and Short BB polymers **(C)**; **(D)** Comparison of the cross-section profiles of the NPs and BB polymers depot at the injection site. Analysis performed with ImageJ software.

After injection, NPs concentrated at the site of injection forming a stable depot (Figure 8B & C), and their distribution appeared to be driven by fluid convection force from the injection itself. No differences were observed between Small and Large NPs (not shown). BB polymers on the other hand, still form a visible depot at the injection site but also appear to diffuse deeply into the brain tissues, displaying a more diffuse pattern (Figure 8C & D).

The BB polymers distribute broadly throughout the cerebral tissue as shown from fluorescence imaging of brain slices and seem to reach tissue regions that are located far away from the injection site. This difference in distribution of NPs and BBs after injection could be related to the superior ability of BBs to diffuse in brain dense ECM [65] or alternatively to use the glymphatic/paravascular pathway. [66]

Conclusions

The shape and mechanical properties of drug carriers are increasingly considered to impact biodistribution and tissue penetration. [42, 67-70] BB polymers, an emerging class of elongated drug carriers, with lengths ranging from 70 to 160 nm were compared *in vitro* and *in vivo* to spherical NPs of similar hydrodynamic sizes. Overall, BB polymers were found to diffuse faster in the ECM compared to NPs but were not captured by surrounding cells, which facilitated their penetration in dense tissues. Due to their much smaller cross-sectional area compared to NPs, BB polymers could infiltrate porous media with small pore size or escape blood vessels by navigating in between endothelial cells. These results were consistently observed both *in vitro* and *in vivo* in different experimental settings and animal species underlying their importance and broad relevance. The AR appears to correlate with the diffusion coefficient of the BB polymers in the gel (Figure 5), while the cell uptake and the overall biodistribution were not correlated to the AR. This is in contrast with results obtained from tobacco mosaic virus showing strong correlation between AR and biodistribution.The differences could originate from the smaller range of AR explored in the present study (2.9 to 6.7) compared to 3.5 to 16.5.[22]

The specific set of attributes found for the set of BB polymers presented here suggest multiple applications as drug delivery systems. As drug carriers, their capacity to broadly distribute in the body allows to significantly increase the distribution volume of drugs, a property that is not achievable with current nanoparticulate systems. The Cy5 fluorescent dye attached to the BB polymer (12 to 14 dye per BB polymer) can mimic a small therapeutic drug. As such the wide distribution of BB polymers showed that these carriers would be good candidates as carriers for middle-sized hydrophobic therapeutic compounds.

In addition, we have seen that the BB polymers can escape efficiently the microvasculature of the brain via passive, intercellular diffusion. This unseen before property makes them excellent candidate for drug delivery systems to the central nervous system which is currently one of the most difficult challenge faced by nanomedicine. Finally, BB polymers' ability to extravasate so efficiently compared to NPs suggest that they have the ability to cross other type of biological barriers such as skin, the gastrointestinal mucosal epithelium or even the eye epithelium. Further studies will confirm if the spectrum of administration routes of BB polymers can be broadened, and which class of drug (small vs large) can benefit most from their attributes as transporters.

Experimental Section

Bottle-brush polymers synthesis

Methyl methacrylate (MMA, purity = 99%, Sigma-Aldrich, USA), 2-(trimethylsilyloxy)ethyl methacrylate (HEMA-TMS, purity > 96%, Scientific Polymer Products Inc., USA) and triethylene glycol methyl ether methacrylate (MEO3MA, purity

= 93%, Sigma Aldrich, USA) were passed through a column filled with basic alumina prior to use.

Tetrahydrofuran (THF) was used after it was purified by tapping off from a solvent purification column. Ethyl α-bromoisobutyrate (EBiB, purity ≥ 98%, Sigma-Aldrich, USA), copper(II) bromide (CuIBr, purity ≥ 99.995% trace metals basis, Sigma-Aldrich, USA), copper(II) chloride (CuIICl2, purity ≥ 99.995% trace metals basis, anhydrous, Sigma-Aldrich, USA), tris(2-pyridylmethyl)amine (TPMA, 98%, Sigma-Aldrich), tris[2-(dimethylamino)ethyl]amine (Me_6TREN, 99%, abcr GmbH), tris(3-hydroxypropyltriazolylmethyl)amine (THPTA, 95%, Sigma Aldrich, USA), potassium fluoride (KF, purity ≥ 99%, spray-dried, Sigma-Aldrich, USA), tetrabutylammonium fluoride (TBAF, 1M solution in THF, Sigma-Aldrich, USA),

Cyanine5 alkyne (Cy5-Alkyne, 95%, Lumiprobe) and α-bromoisobutyryl bromide (purity = 98%, Sigma-Aldrich, USA were used without any additional purification. Milli-Q quality water was obtained from a Millipore Gradient A10 S10 purification system (resistance = 18.2 MΩ.cm, TOC ≤ 4 ppb). Solvents were purchased from Aldrich and used as received without further purification.

Step 1. Synthesis of poly(HEMA-TMS)-co-PMMA.

In a typical procedure, a dry 25 mL Schlenk flask was charged with ethyl α-bromoisobutyrate (EBiB, 12 mg, 0.062 mmol), $Cu^{II}Cl_2$ (1.22 mg, 0.012 mmol), TPMA (10 mg, 0.025 mmol), HEMA-TMS (5.0 g, 5.4 mL, 25 mmol), MMA (2 g, 2.2 mL, 20 mmol) and DMF (1 mL). The solution was degassed by three freeze-pump-thaw cycles. The flask was sealed, evacuated and backfilled with nitrogen five times, and then placed under UV

light. Reaction was stopped when the monomer conversion reached 27.8%. The monomer consumption was calculated by the integration of MMA and HEMA-TMS vinyl groups signal (CHH=C-CH_3, 6.11 ppm or 5.56 ppm) against the internal standard (anisole, o,p-Ar-H, 6.91 ppm). The A block was purified by three precipitations from hexane, dried under vacuum for 16 h at room temperature.

Step 2. Synthesis of polyBiBEM-co-PMMA.

The polymer from step 1 (0.84 g, containing 4.15 mmol of HEMA-TMS units), potassium fluoride (0.289 g, 4.98 mmol) and 2,6-di-tert-butylphenol (86 mg, 0.690 mmol) were placed in a 50 ml round bottom flask. The flask was sealed, flushed with nitrogen, and dry THF (30 mL) was added. The mixture was cooled in an ice bath to 0 °C, tetrabutylammonium fluoride solution in THF (1M, 0.042 mL, 0.04 mmol) was injected to the flask, followed by the drop-wise addition of 2-bromoisobutyryl bromide (0.616 mL, 5.0 mmol) to form the macroinitiator. After the addition the reaction mixture was allowed to reach room temperature and stirring was continued for 24 h. The solids were filtered off, and the solution was precipitated into methanol:water (70:30, v/v%). The precipitated macroinitiator was re-dissolved in chloroform and passed through a short column filled with basic alumina. The filtrate was re-precipitated three times from chloroform into hexanes and dried under vacuum overnight at room temperature.

Step 3. Synthesis of poly[(BiBEM-g-MEO3MA)-stat-MMA] (bottlebrush polymer).

A dry 5 mL Schlenk flask was charged with macroinitiator (14.1 mg, 1.8 μmol of BiBEM), triethylene glycol methyl ether methacrylate (2 g, 8.62 mmol), TPMA (0.9 mg, 0.003 mmol), $Cu^{II}Br_2$ (as a stock solution, 0.2 mg, 0.002 mmol), DMF (0.3 mL) and DMSO (8.0

mL). The solution was degassed by three freeze-pump-thaw cycles. The flask was sealed, evacuated and backfilled with nitrogen five times, and then placed under UV light. The reaction was stopped by exposing the solution to air. The bottlebrush polymer was purified by dialysis against MeOH for 48 h using tubes with a pore size molar mass cut off 10,000 kD. [71]

Step 4. Synthesis of poly[(BiBEM-g-MEO3MA)-stat-MMA]-Azide.

A Schlenk flask was charged with **poly[(BiBEM-g-MEO3MA)-stat-MMA]** (1.0 g, 0.088 × 10-3 mmol), sodium azide (0.023 g, 0.35 mmol), and 10 mL DMF. The reaction mixture was stirred at room temperature for 48 h. The solution was dialyzed against four changes of DMF for 3 days to remove excess sodium azide, and then the DMF solvent in dialysis was replaced with THF. The solution was evaporated and dried under vacuum at room temperature for 24 h.

Step 5. Attachment of Cy5-Alkyne to poly[(BiBEM-g-MEO3MA)-stat-MMA]-Azide

A dry 1.5 mL microcentrifuge vial was charged with poly[(BiBEM-g-MEO3MA)-stat-MMA]-Azide (20 mg, 6.7 nmol) and Cy5-Alkyne (0.09 μmol). The solution was mixed thoroughly and degassed. A degassed solution of $CuSO_4$ (2 mg, 4.67 μmol) and was added. After that, a degassed solution of ascorbic acid (0.8 mg, 4.67 μmol) was added to initiate the reaction and was allowed to run for 12 hours at room temperature with gentle shaking. The product was purified with a 30 kD molecular weight cut-off filter (Millipore). [72]

Bottle-Brush polymers characterization

Proton nuclear magnetic resonance (^{1}H NMR) spectroscopy was performed using Bruker 300 MHz spectrometer. In all cases deuterated chloroform ($CDCl_3$) was used as a solvent,

except for bottle-brush polymer which was analyzed using deuterated methanol (CD_3OD). ^1H chemical shifts are reported in parts per million (ppm) downfield from tetramethylsilane (TMS). Apparent molecular weights and molecular weight distributions measurements of polymers except bottle-brush polymer were measured by size exclusion chromatography (SEC) using Polymer Standards Services (PSS) columns (guard, 105, 103, and 500 Å), with THF or DMF as eluent at 35°C at a constant flow rate of 1.00 mL/min, and differential refractive index (RI) detector (Waters). The apparent number-average molecular weights (*Mn*) and molecular weight distributions (*Mw/Mn*) were determined with a calibration based on linear poly(methyl methacrylate) (PMMA) standards and toluene as an internal standard.

Atomic Force Microscopy (Bottle-brush polymers only): 50 μL of diluted polymer solution in pure water were deposited on freshly cleaved mica surface. After drying, imaging was performed on a Multimode Dimension 3100 AFM equipped with nanoscope VIIIcontroller (Digital instruments) in the peak force QNM mode. Scanasyst-air silicon tips were used for imaging. Individual BBs contour sizes were measured using ImageJ software. [73]

Diblock polymer synthesis and nanoparticle preparation

PLA-*b*-PEG diblocks synthesis was described elsewhere [27]. Briefly Poly(ethylene glycol) monomethyl ether (mPEG) 2kD or mPEG 5kD with a single terminal OH group were used as macroinitiator for 1,8-diazabicyclo[5.4.0]undec-7-ene (DBU) catalyzed Ring-Opening Polymerization of 3,6-Dimethyl-1,4-dioxane-2,5-dione to Poly(lactic acid) (PLA). After purification by repeated precipitation in cold methanol, diblock polymers were characterized by GPC and ^1H NMR. Nanoparticle preparation was performed by

nanoprecipitation as previously described. [28, 74] Briefly, an organic solution (acetone with the diblock polymer mixed with PLA functionalized with fluorophore Cy5) and pure water were introduced separately in an impinging jet mixer at identical flow rates. After nanosuspension recovery and solvent removal by dialysis, the obtained NPs were characterized for size by Differential Dynamic Microscopy and TEM as described below.

BB polymer and NP size measurement

Zeta potential (NPs)

Zeta potential (ζ) of NPs and BB polymers were measured in NaCl 5 mM using disposable folded capillary cells on a Zetasizer Nano-ZS (Malvern Instruments, Worchester, UK), using the Smoluchowski approach.

TEM (NPs only)

Transmission Electron Microscopy (TEM) imaging was made at INRS Centre Armand-Frappier Characterization platform for nanovehicles (Laval, Qc Canada) on a Hitachi H-7100 (Hitachi, Japan) at x 10 000 and x 50 000 magnifications. NPs suspended in MilliQ water were deposited on a copper grid and air-dried. The grids were treated with one drop of 3% (w/v) phosphotungstic acid. After air-drying, grids were loaded in the instrument and imaged.

Differential Dynamic Microscopy (NPs and BBs)

Differential Dynamic Microscopy (DDM) size measurements were performed on borosilicate capillaries (VitroCom, USA) filled with freshly filtrated aqueous suspensions of NPs or BBs (0.45 µm nylon filter, Millex, Millipore USA) and sealed using petroleum jelly. Videos were acquired on an upright microscope (Olympus BX81, Japan) equipped

with a high acquisition speed camera (Hamamatsu Orca-Flash 4.0 V3, Japan). Phase-contrast imaging and x20 magnification were used. Videos were recorded at a framerate of 100 fps, with an image binning of 1x1 within a region of interest of 512 x 512 pixels. For each sample, five different videos were recorded at different positions in the capillary.

Videos analysis was performed as previously described. [38] Briefly, the power spectra of the differences between pairs of images separated by a delay time τ were computed and averaged to obtain the differential image correlation function $g(q,\tau)$, with q the spatial frequency. Under appropriate imaging conditions, $g(q,\tau)$ is related to the intermediate scattering function (ISF) $f(q,\tau)$ as:

Eq. 1. $$g(q,\tau) = A(q)\,[1 - f(q,\tau)] + B(q)$$

with $A(q)$ the signal amplitude and $B(q)$ the instrumental noise. To assess particles dynamics, $g(q,\tau)$ can then be fitted with adequate models for the ISF. For size measurements, we used the cumulants method. [75, 76] The diffusion coefficients D were extracted and allowed to estimate the hydrodynamic diameters using the Stokes-Einstein equation:

Eq. 2. $$D = k_B T / 6\eta r_H.$$

Endocytosis: flow cytometry experiment

Endocytosis experiments were carried-out as previously described [77] in bEnd.3 cells (murine brain vascular endothelial cell line), N2a (murine neuronal cell line), N11 (murine microglia cell line) and Huvec (Human Umbilical vascular endothelial cells). Detailed experimental procedures can be found in Supporting Information file.

In vitro cell barrier translocation experiments

Establishment of the i*n vitro* Transwell BBB transcytosis/translocation model was described previously. [77] Detailed procedures regarding brain vascular endothelial cell monolayer permeability assessment, immunodetection of tight junction proteins and confocal imaging of vascular endothelial cell monolayer can be found in Supporting Information file.

The transcytosis experiments were carried out in a complete medium (with 10% FBS) devoid of phenol red. Identical doses of NPs or BBs (24µg in 350µl in the apical compartment) were incubated for 24 and 48 hours. After 24 or 48 h media were collected and transferred in a 96-well black clear bottom plates and fluorescence of Cy5 (λexc. 640/λem. 670nm) was read SpectraMax M5 fluorescence plate reader (Molecular Devices, USA). NPs and BB polymers translocation was quantified by the mean fluorescence intensity of the apical and basal compartment media and normalized to the intensity at t = 0. Quantification of passage (µg) was calculated from an external calibration curve performed in complete cell culture medium and converted into apparent permeability coefficients (P_{app}) according to Eq. 3 for direct comparison.

The apparent permeability (P_{app}) of monolayer bEnd.3 cells on Transwell was calculated from the following equation:

Eq. 3 $$P_{app} = \frac{V_R \, \Delta C_R}{\Delta t \, S_{ins} C_D}$$

With *Papp* apparent permeability (cm.s^{-1}); V_R, volume of receiving compartment (cm^3), ΔC_R, change in concentration in the receiving compartment (µg/mL); Δt, time in seconds

(s); S_{ins}: surface of the insert (cm^2) and C_D: concentration in the donor compartment (µg/mL).

On-chip vascular permeability assay

Microfluidic device design

The microfluidic device was designed following the protocols available in the literature. [78, 79] Briefly, the device consists of three diamond-shaped (1 mm × 2 mm × 0.1-0.12 mm) tissue chambers that are interconnected in the longitudinal direction. Two microfluidic lines (0.1 mm × 0.1-0.12 mm) are connected to the tissue chambers on either side via a connecting pore (50 μm), as shown in Figure S7A. The connecting pore is designed with a curved opening that stimulates a flat gel boundary close enough to the straight microfluidic channel to enhance the anastomosis of the vascular network in the tissue chambers. The side fluidic lines accommodate the culture medium flow during the tissue growth and, nanoparticles flow during the nanomedicine diffusion analysis. To stimulate the flow, a large reservoir is attached on top of each inlet and outlet of the microfluidic lines, furnishing 5-mm H_2O hydrostatic and 5-mm H_2O interstitial pressure across the microfluidic channels and tissue chambers, respectively. Therefore, the culture media flowed in opposite directions in the two microfluidic channels.

A pressure regulator is designed between the cell seeding port and tissue chambers to ensure a robust loading of the cell-hydrogel mixture inside the tissue chambers while preventing its entry into the side microfluidic channels. As shown in Figure S7B & C, the widths of pressure releasing safety microvalves (60 μm) are larger than the widths of connecting pores between the tissue chambers and microfluidic lines (50 μm). This design criterium ensures that, in the presence of excessive pressure during cell loading, the safety

microvalves will burst before the connecting pores, confining the cell-gel mixture to the tissue chambers. [78, 79]

Microfluidic chip fabrication

Standard soft-lithographic techniques were used to fabricate the microfluidic devices. Detailed microfabrication procedures, sterilization and testing can be found in Supporting Information file.

Cell culture, seeding the device and maintaining the vascular-on-a-chip model

Human umbilical vein endothelial cell (HUVEC) and normal human lung fibroblast (NHLF) were purchased from Lonza, cultured in EGM-2 (Lonza) and FGM-2 (Lonza) and used at passage 4 and 6, respectively. Fibrinogen solution was prepared by dissolving 75% clottable bovine fibrinogen (Sigma-Aldrich) in 1× Dulbecco's Phosphate Buffered Saline with Ca^{2+}/Mg^{2+} (Sigma-Aldrich) at 37℃ to a final concentration of 10 mg/mL. HUVECs and NHLFs were harvested and mixed each at a concentration of 5×10^6 cells/mL. The culture medium was aspirated, and the cell mixture was resuspended in the fibrinogen solution.

The final cell-matrix suspension was mixed with human plasma thrombin (50 U/mL, Millipore Canada Ltd.) to a final concentration of 3 U/mL. 10 μl of the final cell-matrix pregel solution was quickly seeded into the microtissue chambers and allowed to polymerize in a 37°C incubator for 30 minutes. Next, laminin (1 mg/mL from Engelbreth-Holm-Swarm lathrytic mouse tumor, Corning Incorporated) was loaded into the microfluidic channels through the medium inlets and incubated at 37 °C for another 15 minutes to stimulate HUVEC anastomosis with the microfluidic channels. 500 μl of culture medium (EGM-2, Lonza) was introduced into the microfluidic channels and subsequently

medium reservoirs. The culture medium with complete growth factors was replaced with the culture medium without VEGF and hFGF growth factors 24 hours after initial seeding. The culture media were changed and leveled every other day to maintain interstitial flow and the direction of the flows were reversed every 3 days, to ensure a symmetrical cellular outgrowth in the side microfluidic channels.

Nanoparticle and bottle-brushes diffusion in vascular-on-chip model

To study NPs and BBs diffusion, medium is replaced by DPBS with similar hydrostatic pressure profile (i.e., 500 μl of DPBS), and the device is positioned onto a microscope stage. In one microfluidic side channel, NPs or BBs suspension was introduced to the reservoir with highest hydrostatic pressure to achieve a final concentration of 50 μg/mL, and time-lapse images of the nanocarrier diffusion across the tissue chamber were acquired. The image analysis was performed using ImageJ. [73]

Diffusion of NPs and BBs in extracellular matrix emulating hydrogels

Preparation of gels

Fibrin hydrogels were prepared with final concentrations of 10 mg/mL fibrinogen, 3 U/mL thrombin, and 0.4 mg/mL brushes (small or medium) or 1 mg/mL NPs (NP PEG2000). Suspensions of brushes and NPs were freshly filtered on 0.45µm nylon filter prior to hydrogel preparation. PBS 1X without Ca^{2+}/Mg^{2+} was used as the medium. After mixing, the pregel solution was quickly injected in a capillary, left to gel during 30 min in a humidified incubator at 37°C, and then sealed using petroleum jelly. Preliminary data obtained for different incubation times ensured that the gel was stabilized after 30 min.

Prior to any measurement, the gel was stabilized at room temperature during another 30 min, as temperature greatly impacts the diffusion process.

DDM procedures & analyses

DDM measurements were performed at five different positions in the gel to take into account a possible heterogeneity. Videos were acquired with the same parameters as for size measurements, except an image binning of 2x2 was used to increase the signal amplitude. Data analysis was also performed in a similar way, except we chose the generalized exponential form of the ISF to fit the data:

Eq. 4

$$f(q,\tau) = e^{-(\frac{\tau}{\tau_R})^{\beta}}$$

with β the stretch exponent and τ_R the relaxation time, from which the effective isotropic diffusion coefficient D can be extracted through:

Eq. 5

$$\tau_R = \frac{1}{q^2 D}$$

In vivo Zebrafish experiments

All zebrafish (*Danio Rerio*) experimental procedures were conducted in concordance with the Canadian Council on Animal Care (CCAC) guidelines. Tupfel long-in (TL, i.e. wild type), *Tg (vglut2a:RFP)* [49] and *Tg (flk1:EGFP)* transgenic strains [80] were used for *in vivo* distribution experiments. Adult zebrafishes were maintained at 28.5°C and kept under a 12/12 h light/dark cycles at the animal facility of the Laboratoire National de Biologie

Experimentale (LNBE), Laval, Canada. They were bred according to standard procedures and staged as previously described. [81] Eggs were collected and transferred to Petri dishes filled with Fish water and methylene blue. 1-Phenyl-2-thiourea (PTU) was added at 24 hours post-fertilization (hpi) to prevent pigmentation. Petri dishes were placed in an incubator set at 28°C.

Intravenous injections were performed on 48 hpf larvae in the duct of Cuvier as previously described. [27,77] Confocal imaging was performed on a LSM780 confocal microscope (Zeiss Canada Ltd, ON). Only larvae maintaining heartbeat and robust circulation throughout the imaging period were reported. Images were processed with Zeiss Black (Zeiss, Germany) and Imaris 9.2 software (Oxford Instruments, Bitplane Inc. Concord, MA USA).

Assessment of NPs and BB polymers diffusion in mice brain

The experimental procedures were approved by Institutional Animal Care and Use Ethics Committee (IACUC) of INRS in accordance with the Canadian Council on Animal Care (CCAC) guidelines (Protocol number #1803-01). Female mice with a C57BL/6 (WT) background were from a colony (Protocol # 1409-04). Animals were housed at 24 ± 1°C in a 12h light / 12h dark cycle with free access to water and feed with "Teklad global 18% protein rodent diet" (Product reference # 2018; Envigo, Montréal, Canada).

Two to four months-old female mice were anesthetized with an intraperitoneal injection of ketamin/xylazin mixture (respectively 100mg/kg and 10mg/kg). Briefly, mice were placed into a stereotaxic table and fluorescent NPs and BB polymers were injected unilaterally into the lateral ventricle (LV) or in CA1 field of the hippocampus (HI) with a Hamilton syringe (Model 1701 N, Hamilton, NV, USA).

The injections into the LV were performed with the stereotaxic coordinates defined as 0.3 mm posterior from the bregma, 1.0 mm lateral to the sagittal suture, and 2.5 mm below the skull surface. [82] For the injections in the CA1, the stereotaxic coordinates were: 2.00 mm posterior from the bregma, 1.8 mm lateral to the sagittal suture and 1.5 mm below the skull surface. [83, 84]

3 µl of fluorescent BBs (2 mg/mL) or 2 µl of fluorescent PEGylated NPs (3 mg/mL) for equivalent quantity of material in weight were injected at a rate of 0.2 µl/min. After injection the needle remained in position for 5 min and then was slowly removed.

Brain extraction, fixation, and slices preparation

Mice were maintained under sedation with ketamine/xylazine during 1 hour after completion of the brain injection. They were then transcardially perfused with 20 ml of 0.9 % NaCl for 10 minutes, followed by a perfusion of PFA 4% diluted in PBS. The brains were removed and kept in an ice-cold 4% PFA/PBS and kept at 4°C for 24 hours then transferred in 15 mL of 15% sucrose/PBS at 4°C until brain sink to the bottom of the tube. This step was repeated with 30% sucrose/PBS. Before snap frozen, the brains were quickly dried with paper, immersed in cold isopentane for few seconds, and stored at -80°C prior to use.

Frozen brains were equilibrated at -20°C and embedded in Tissue Freezing Medium (Triangle Biomedial Sciences, Durham, NC USA) and 20 µm thin sections were cut with a rotary microtome (Microtome Cryostat HM525, Microm International GmbH, Germany) and gently deposited on glass slides (Glass slide Superfrost Plus, Fisherbrand, USA). Brain slices were fixed again with PFA 4% in PBS for 15 minutes. After three washings in 0.1%

Tween 20 in PBS with Ca^{2+}/Mg^{2+}, brain slices were stained with Hoechst 33342 (ThermoFisher Scientific, Canada) to reveals cell nucleus, and next washed again three times with PBS.

Complete coronal sections were imaged on a Cytation5 (BioTek, Canada). For confocal imaging brain slices were mounted with cover glass using Prolong® Antifade mounting medium (ThermoFisher scientific, Canada). Confocal images were acquired on a LSM780 confocal microscope (Zeiss Canada Ltd, ON).

Statistical analysis

Endocytosis data were tested for significance using SigmaPlot® 12.0 (Systat Software). Comparison of multiple groups was performed by One-way Anova using the Holm Sidak test ($p<0.05$). Number of replicate are indicated in figure legends.

ASSOCIATED CONTENT

Supporting Information

Supporting information to this article is available free of charge at: https://…

BB Polymers characterizations (GPC, NMR); BB polymers contour length measurement from AFM; NP and BBs fluorescence levels assessment and calibration; NPs and BBs cytotoxicity assays in vitro; NPs and BBs cell uptake at 4 hours in three different cell lines; Effect of temperature on transcytosis of BB polymers; Detailed microvessels-on-chip device fabrication and validation; Supplementary zebrafish larvae confocal images: NPs and BBs biodistribution at 24 hpi, Dextrans 10kD, 150 kD and 2MD, Short and Medium BBs biodistribution at 1 and 24 hours, z-stack movies of Head and trunk of WT larvae injected with Long BBs, NPs and Long BBs biodistribution and brain colocalization in Tg (vglu2a:RFP) transgenic zebrafish larvae; Mouse brain injection: Brain maps showing the localisation of injections sites, confocal images after ICV injection of NPs and Short BBs. Z-stack movies of WT zebrafish larvae brain after injection with Long BB polymers, 2hpi (Movie 1) and WT zebrafish larvae trunk after injection with Long BB polymers, 2hpi (Movie 2)

Author contributions

JMR: Conceptualization; Investigation; Methodology; Writing: original draft; Writing: Reviewing & editing; MM: Conceptualization; Investigation; Methodology; Writing: original draft; MO: Investigation; Methodology; Writing: original draft; GX: Investigation; Methodology; MLG: Investigation; Methodology; Writing: original draft - review & editing; PLL**:** Investigation; Methodology; Writing - review & editing; HC: Investigation; Methodology; Writing - review & editing; VH: Investigation; Methodology; ROS: Investigation; CZ: Investigation; VA: Investigation; MA: Investigation; MS: Supervision; VM: Supervision, Writing – Reviewing and editing; SAP: Supervision, Writing – Reviewing and editing; KM: Supervision, Funding acquisition, Writing – Reviewing and editing; CR: Supervision, Funding acquisition, Writing – Reviewing and editing; XB: Supervision, Funding acquisition, Conceptualization; Writing - original draft; Writing – Reviewing and editing.

* JMR & MM contributed equally to this work.

Notes

The authors declare no competing financial interest.

ACKNOWLEDGMENTS

JMR thanks NSERC/CRSNG (Government of Canada) for postdoctoral fellowship (2017-2019). This research was undertaken thanks, in part, to funding from the Canada First Research Excellence Fund through the TransMedTech Institute (Postdoctoral fellowships, JMR; MM & MLG). MLG acknowledges FRQS for financial support. CR acknowledges funding from NSERC/CRSNG (Government of Canada) and the Research Chair on Alzheimer's disease. XB acknowledges the support from the Canada Research Chair program, from FRQS under the umbrella of ERA-NET EuroNanoMed (GA N°723770) of the EU Horizon 2020 Research and Innovation Program and the FRQNT (Team grant) and NSERC/CRSNG (Discovery grant). SAP acknowledges funding from Canadian Institute of Health Research, NSERC/CRSNG and Canada Foundation for Innovation.

Tg (flk1:EGFP) was a generous gift from Dr. Xiao-Yan Wen (U. of Toronto, Toronto, ON Canada). Zoé Butti and Pryanka Jamadagni are gratefully acknowledged for their help in zebrafish husbandry and crossing (SA. Patten lab); Jessy Tremblay (Confocal Microscopy and Flux Cytometry Laboratory, INRS) for his help with larvae imaging; Christian Charbonneau and the IRIC Bio-imaging core facility (Montreal, Qc) for help with image treatment.

REFERENCES

1. Crommelin, D. J.; Florence, A. T., Towards more effective advanced drug delivery systems. *Int J Pharm* **2013,** *454* (1), 496-511.
2. Wilhelm, S.; Tavares, A. J.; Dai, Q.; Ohta, S.; Audet, J.; Dvorak, H. F.; Chan, W. C. W., Analysis of nanoparticle delivery to tumours. *Nat, Rev. Mat.* **2016,** *1* (5), 16014.
3. Bae, Y. H.; Park, K., Targeted drug delivery to tumors: myths, reality and possibility. *J. Control. Release* **2011,** *153* (3), 198-205.
4. Kirpotin, D. B.; Drummond, D. C.; Shao, Y.; Shalaby, M. R.; Hong, K.; Nielsen, U. B.; Marks, J. D.; Benz, C. C.; Park, J. W., Antibody targeting of long-circulating lipidic nanoparticles does not increase tumor localization but does increase internalization in animal models. *Cancer Res.* **2006,** *66* (13), 6732-40.
5. Sindhwani, S.; Syed, A. M.; Ngai, J.; Kingston, B. R.; Maiorino, L.; Rothschild, J.; MacMillan, P.; Zhang, Y.; Rajesh, N. U.; Hoang, T.; Wu, J. L. Y.; Wilhelm, S.; Zilman, A.; Gadde, S.; Sulaiman, A.; Ouyang, B.; Lin, Z.; Wang, L.; Egeblad, M.; Chan, W. C. W., The entry of nanoparticles into solid tumours. *Nat Mater* **2020,** *19* (5), 566-575.
6. Delbreil, P.; Rabanel, J.-M.; Banquy, X.; Brambilla, D., Therapeutic nanotechnologies for Alzheimer's disease: A critical analysis of recent trends and findings. *Adv. Drug Del. Rev.* **2022,** *187*, 114397.
7. Ding, J.; Chen, J.; Gao, L.; Jiang, Z.; Zhang, Y.; Li, M.; Xiao, Q.; Lee, S. S.; Chen, X., Engineered nanomedicines with enhanced tumor penetration. *Nano Today* **2019,** *29*, 100800.
8. Stylianopoulos, T.; Poh, M. Z.; Insin, N.; Bawendi, M. G.; Fukumura, D.; Munn, L. L.; Jain, R. K., Diffusion of particles in the extracellular matrix: the effect of repulsive electrostatic interactions. *Biophys. J.* **2010,** *99* (5), 1342-9.
9. Le Goas, M.; Testard, F.; Tache, O.; Debou, N.; Cambien, B.; Carrot, G.; Renault, J. P., How Do Surface Properties of Nanoparticles Influence Their Diffusion in the Extracellular Matrix? A Model Study in Matrigel Using Polymer-Grafted Nanoparticles. *Langmuir* **2020,** *36* (35), 10460-10470.
10. Xie, G.; Martinez, M. R.; Olszewski, M.; Sheiko, S. S.; Matyjaszewski, K., Molecular Bottlebrushes as Novel Materials. *Biomacromolecules* **2019,** *20* (1), 27-54.
11. Lee, H. I.; Pietrasik, J.; Sheiko, S. S.; Matyjaszewski, K., Stimuli-responsive molecular brushes. *Prog. Polym. Sci.* **2010,** *35* (1-2), 24-44.
12. Johnson, J. A.; Lu, Y. Y.; Burts, A. O.; Xia, Y.; Durrell, A. C.; Tirrell, D. A.; Grubbs, R. H., Drug-loaded, bivalent-bottle-brush polymers by graft-through ROMP. *Macromolecules* **2010,** *43* (24), 10326-10335.
13. Huang, K.; Jacobs, A.; Rzayev, J., De novo synthesis and cellular uptake of organic nanocapsules with tunable surface chemistry. *Biomacromolecules* **2011,** *12* (6), 2327-34.
14. Xia, Y.; Adibnia, V.; Huang, R.; Murschel, F.; Faivre, J.; Xie, G.; Olszewski, M.; De Crescenzo, G.; Qi, W.; He, Z.; Su, R.; Matyjaszewski, K.; Banquy, X., Biomimetic Bottlebrush Polymer Coatings for Fabrication of Ultralow Fouling Surfaces. *Angew Chem Int Ed Engl* **2019,** *58* (5), 1308-1314.
15. Banquy, X.; Burdynska, J.; Lee, D. W.; Matyjaszewski, K.; Israelachvili, J., Bioinspired bottle-brush polymer exhibits low friction and Amontons-like behavior. *J. Am. Chem. Soc.* **2014,** *136* (17), 6199-202.
16. Mullner, M.; Dodds, S. J.; Nguyen, T. H.; Senyschyn, D.; Porter, C. J.; Boyd, B. J.; Caruso, F., Size and rigidity of cylindrical polymer brushes dictate long circulating properties in vivo. *ACS Nano* **2015,** *9* (2), 1294-304.
17. Chariou, P. L.; Lee, K. L.; Pokorski, J. K.; Saidel, G. M.; Steinmetz, N. F., Diffusion and Uptake of Tobacco Mosaic Virus as Therapeutic Carrier in Tumor Tissue: Effect of Nanoparticle Aspect Ratio. *J Phys Chem B* **2016,** *120* (26), 6120-9.

18. Zhao, J.; Lu, H.; Xiao, P.; Stenzel, M. H., Cellular Uptake and Movement in 2D and 3D Multicellular Breast Cancer Models of Fructose-Based Cylindrical Micelles That Is Dependent on the Rod Length. *ACS Appl Mater Interfaces* **2016,** *8* (26), 16622-30.
19. Müllner, M.; Yang, K.; Kaur, A.; New, E. J., Aspect-ratio-dependent interaction of molecular polymer brushes and multicellular tumour spheroids. *Polymer Chemistry* **2018,** *9* (25), 3461-3465.
20. Yu, Q.; Roberts, M. G.; Houdaihed, L.; Liu, Y.; Ho, K.; Walker, G.; Allen, C.; Reilly, R. M.; Manners, I.; Winnik, M. A., Investigating the influence of block copolymer micelle length on cellular uptake and penetration in a multicellular tumor spheroid model. *Nanoscale* **2021,** *13* (1), 280-291.
21. Zhang, Z.; Zhang, L.; Zhao, J.; Li, C.; Wu, W.; Jiang, X., Length effects of cylindrical polymer brushes on their in vitro and in vivo properties. *Biomater Sci* **2019,** *7* (12), 5124-5131.
22. Shukla, S.; Eber, F. J.; Nagarajan, A. S.; DiFranco, N. A.; Schmidt, N.; Wen, A. M.; Eiben, S.; Twyman, R. M.; Wege, C.; Steinmetz, N. F., The Impact of Aspect Ratio on the Biodistribution and Tumor Homing of Rigid Soft-Matter Nanorods. *Adv Healthc Mater* **2015,** *4* (6), 874-82.
23. Pizzi, D.; Mahmoud, A. M.; Klein, T.; Morrow, J. P.; Humphries, J.; Houston, Z. H.; Fletcher, N. L.; Bell, C. A.; Thurecht, K. J.; Kempe, K., Poly(2-ethyl-2-oxazoline) bottlebrushes: How nanomaterial dimensions can influence biological interactions. *Eur. Polym. J.* **2021,** *151*, 110447.
24. Mullner, M.; Mehta, D.; Nowell, C. J.; Porter, C. J., Passive tumour targeting and extravasation of cylindrical polymer brushes in mouse xenografts. *Chem Commun (Camb)* **2016,** *52* (58), 9121-4.
25. Peer, D.; Karp, J. M.; Hong, S.; Farokhzad, O. C.; Margalit, R.; Langer, R., Nanocarriers as an emerging platform for cancer therapy. *Nat. Nanotech.* **2007,** *2* (12), 751-760.
26. Mitchell, M. J.; Billingsley, M. M.; Haley, R. M.; Wechsler, M. E.; Peppas, N. A.; Langer, R., Engineering precision nanoparticles for drug delivery. *Nature Reviews Drug Discovery* **2021,** *20* (2), 101-124.
27. Rabanel, J. M.; Piec, P. A.; Landri, S.; Patten, S. A.; Ramassamy, C., Transport of PEGylated-PLA nanoparticles across a blood brain barrier model, entry into neuronal cells and in vivo brain bioavailability. *J. Control. Release* **2020,** *328*, 679-695.
28. Rabanel, J. M.; Faivre, J.; Tehrani, S. F.; Lalloz, A.; Hildgen, P.; Banquy, X., Effect of the Polymer Architecture on the Structural and Biophysical Properties of PEG-PLA Nanoparticles. *ACS Appl Mater Interfaces* **2015,** *7* (19), 10374-85.
29. Neugebauer, D.; Sumerlin, B. S.; Matyjaszewski, K.; Goodhart, B.; Sheiko, S. S., How dense are cylindrical brushes grafted from a multifunctional macroinitiator? *Polymer* **2004,** *45* (24), 8173-8179.
30. Sheiko, S. S.; Sun, F. C.; Randall, A.; Shirvanyants, D.; Rubinstein, M.; Lee, H.-i.; Matyjaszewski, K., Adsorption-induced scission of carbon–carbon bonds. *Nature* **2006,** *440* (7081), 191-194.
31. Rabanel, J. M.; Hildgen, P.; Banquy, X., Assessment of PEG on polymeric particles surface, a key step in drug carrier translation. *J. Control. Release* **2014,** *185* (0), 71-87.
32. Watanabe, T.; Dohgu, S.; Takata, F.; Nishioku, T.; Nakashima, A.; Futagami, K.; Yamauchi, A.; Kataoka, Y., Paracellular barrier and tight junction protein expression in the immortalized brain endothelial cell lines bEND.3, bEND.5 and mouse brain endothelial cell 4. *Biol. Pharm. Bull.* **2013,** *36* (3), 492-5.
33. Klebe, R. J.; Ruddle, R. H., Neuroblastoma - Cell Culture Analysis of a Differentiating Stem Cell System. *J. Cell Biol.* **1969,** *43* (2p2), A69-&.

34. Righi, M.; Mori, L.; De Libero, G.; Sironi, M.; Biondi, A.; Mantovani, A.; Donini, S. D.; Ricciardi-Castagnoli, P., Monokine production by microglial cell clones. *Eur. J. Immunol.* **1989,** *19* (8), 1443-8.
35. Street, S. T. G.; He, Y.; Jin, X. H.; Hodgson, L.; Verkade, P.; Manners, I., Cellular uptake and targeting of low dispersity, dual emissive, segmented block copolymer nanofibers. *Chem. Sci.* **2020,** *11* (32), 8394-8408.
36. Ribovski, L.; de Jong, E.; Mergel, O.; Zu, G.; Keskin, D.; van Rijn, P.; Zuhorn, I. S., Low nanogel stiffness favors nanogel transcytosis across an in vitro blood-brain barrier. *Nanomed. Nanotechnol. Biol. Med.* **2021,** *34*, 102377.
37. Smith, M.; Poling-Skutvik, R.; Slim, A. H.; Willson, R. C.; Conrad, J. C., Dynamics of Flexible Viruses in Polymer Solutions. *Macromolecules* **2021,** *54* (10), 4557-4563.
38. Latreille, P. L.; Adibnia, V.; Nour, A.; Rabanel, J. M.; Lalloz, A.; Arlt, J.; Poon, W. C. K.; Hildgen, P.; Martinez, V. A.; Banquy, X., Spontaneous shrinking of soft nanoparticles boosts their diffusion in confined media. *Nat Commun* **2019,** *10* (1), 4294.
39. Doi, M.; Edwards, S. F., *The theory of polymer dynamics*. Clarendon Press: Oxford [Oxfordshire], 1988, p 391.
40. Teraoka, I., Dynamics of Dilute Polymer Solutions. In *Polymer Solutions*, John Wiley & Sons, Inc., New York, 2002; pp 167-275.
41. Pluen, A.; Netti, P. A.; Jain, R. K.; Berk, D. A., Diffusion of macromolecules in agarose gels: comparison of linear and globular configurations. *Biophys. J.* **1999,** *77* (1), 542-52.
42. Bao, C.; Liu, B.; Li, B.; Chai, J.; Zhang, L.; Jiao, L.; Li, D.; Yu, Z.; Ren, F.; Shi, X.; Li, Y., Enhanced Transport of Shape and Rigidity-Tuned alpha-Lactalbumin Nanotubes across Intestinal Mucus and Cellular Barriers. *Nano Lett.* **2020,** *20* (2), 1352-1361.
43. Wang, J. L.; O'Connor, T. C.; Grest, G. S.; Zheng, Y. T.; Rubinstein, M.; Ge, T., Diffusion of Thin Nanorods in Polymer Melts. *Macromolecules* **2021,** *54* (15), 7051-7059.
44. Lee, J.; Grein-Iankovski, A.; Narayanan, S.; Leheny, R. L., Nanorod Mobility within Entangled Wormlike Micelle Solutions. *Macromolecules* **2017,** *50* (1), 406-415.
45. Wang, J. L.; Yang, Y. W.; Yu, M. R.; Hu, G. Q.; Gan, Y.; Gao, H. J.; Shi, X. H., Diffusion of rod-like nanoparticles in non-adhesive and adhesive porous polymeric gels. *J. Mech. Phys. Solids* **2018,** *112*, 431-457.
46. Sieber, S.; Grossen, P.; Bussmann, J.; Campbell, F.; Kros, A.; Witzigmann, D.; Huwyler, J., Zebrafish as a preclinical in vivo screening model for nanomedicines. *Adv. Drug Del. Rev.* **2019,** *151-152*, 152-168.
47. Sieber, S.; Grossen, P.; Detampel, P.; Siegfried, S.; Witzigmann, D.; Huwyler, J., Zebrafish as an early stage screening tool to study the systemic circulation of nanoparticulate drug delivery systems in vivo. *J. Control. Release* **2017,** *264*, 180-191.
48. Dal, N. K.; Kocere, A.; Wohlmann, J.; Van Herck, S.; Bauer, T. A.; Resseguier, J.; Bagherifam, S.; Hyldmo, H.; Barz, M.; De Geest, B. G.; Fenaroli, F., Zebrafish Embryos Allow Prediction of Nanoparticle Circulation Times in Mice and Facilitate Quantification of Nanoparticle-Cell Interactions. *Small* **2020,** *16* (5), e1906719.
49. Satou, C.; Kimura, Y.; Hirata, H.; Suster, M. L.; Kawakami, K.; Higashijima, S., Transgenic tools to characterize neuronal properties of discrete populations of zebrafish neurons. *Development* **2013,** *140* (18), 3927-31.
50. Henson, H. E.; Parupalli, C.; Ju, B.; Taylor, M. R., Functional and genetic analysis of choroid plexus development in zebrafish. *Front. Neurosci.* **2014,** *8* (364), 364.
51. Jeong, J. Y.; Kwon, H. B.; Ahn, J. C.; Kang, D.; Kwon, S. H.; Park, J. A.; Kim, K. W., Functional and developmental analysis of the blood-brain barrier in zebrafish. *Brain Res. Bull.* **2008,** *75* (5), 619-28.

52. Naseri Kouzehgarani, G.; Feldsien, T.; Engelhard, H. H.; Mirakhur, K. K.; Phipps, C.; Nimmrich, V.; Clausznitzer, D.; Lefebvre, D. R., Harnessing cerebrospinal fluid circulation for drug delivery to brain tissues. *Adv Drug Deliv Rev* **2021,** *173*, 20-59.
53. Iliff, J. J.; Wang, M.; Liao, Y.; Plogg, B. A.; Peng, W.; Gundersen, G. A.; Benveniste, H.; Vates, G. E.; Deane, R.; Goldman, S. A.; Nagelhus, E. A.; Nedergaard, M., A Paravascular Pathway Facilitates CSF Flow Through the Brain Parenchyma and the Clearance of Interstitial Solutes, Including Amyloid β. *Sci. Transl. Med.* **2012,** *4* (147), 147ra111-147ra111.
54. Pardridge, W. M., CSF, blood-brain barrier, and brain drug delivery. *Expert Opin Drug Deliv* **2016,** *13* (7), 963-75.
55. Mestre, H.; Mori, Y.; Nedergaard, M., The Brain's Glymphatic System: Current Controversies. *Trends Neurosci.* **2020,** *43* (7), 458-466.
56. Liu, X.; Ramirez, S.; Pang, P. T.; Puryear, C. B.; Govindarajan, A.; Deisseroth, K.; Tonegawa, S., Optogenetic stimulation of a hippocampal engram activates fear memory recall. *Nature* **2012,** *484* (7394), 381-5.
57. Ramirez, S.; Liu, X.; Lin, P. A.; Suh, J.; Pignatelli, M.; Redondo, R. L.; Ryan, T. J.; Tonegawa, S., Creating a false memory in the hippocampus. *Science* **2013,** *341* (6144), 387-91.
58. Milner, B.; Klein, D., Loss of recent memory after bilateral hippocampal lesions: memory and memories-looking back and looking forward. *J Neurol Neurosurg Psychiatry* **2016,** *87* (3), 230.
59. Josephy-Hernandez, S.; Pirvulescu, I.; Maira, M.; Aboulkassim, T.; Wong, T. P.; McKinney, R. A.; Saragovi, H. U., Pharmacological interrogation of TrkA-mediated mechanisms in hippocampal-dependent memory consolidation. *PLoS One* **2019,** *14* (6), e0218036.
60. Hollnagel, J. O.; Elzoheiry, S.; Gorgas, K.; Kins, S.; Beretta, C. A.; Kirsch, J.; Kuhse, J.; Kann, O.; Kiss, E., Early alterations in hippocampal perisomatic GABAergic synapses and network oscillations in a mouse model of Alzheimer's disease amyloidosis. *PLoS One* **2019,** *14* (1), e0209228.
61. Gengler, S.; Hamilton, A.; Holscher, C., Synaptic plasticity in the hippocampus of a APP/PS1 mouse model of Alzheimer's disease is impaired in old but not young mice. *PLoS One* **2010,** *5* (3), e9764.
62. Li, S.; Jin, M.; Koeglsperger, T.; Shepardson, N. E.; Shankar, G. M.; Selkoe, D. J., Soluble Abeta oligomers inhibit long-term potentiation through a mechanism involving excessive activation of extrasynaptic NR2B-containing NMDA receptors. *J Neurosci* **2011,** *31* (18), 6627-38.
63. Parsons, M. P.; Raymond, L. A., Extrasynaptic NMDA receptor involvement in central nervous system disorders. *Neuron* **2014,** *82* (2), 279-93.
64. Palop, J. J.; Mucke, L., Epilepsy and cognitive impairments in Alzheimer disease. *Arch Neurol* **2009,** *66* (4), 435-40.
65. Thorne, R. G.; Nicholson, C., In vivo diffusion analysis with quantum dots and dextrans predicts the width of brain extracellular space. *Proc. Natl. Acad. Sci. USA* **2006,** *103* (14), 5567-72.
66. Gu, X.; Song, Q.; Zhang, Q.; Huang, M.; Zheng, M.; Chen, J.; Wei, D.; Chen, J.; Wei, X.; Chen, H.; Zheng, G.; Gao, X., Clearance of two organic nanoparticles from the brain via the paravascular pathway. *J. Control. Release* **2020,** *322*, 31-41.
67. Chauhan, V. P.; Popovic, Z.; Chen, O.; Cui, J.; Fukumura, D.; Bawendi, M. G.; Jain, R. K., Fluorescent nanorods and nanospheres for real-time in vivo probing of nanoparticle shape-dependent tumor penetration. *Angew Chem Int Ed Engl* **2011,** *50* (48), 11417-20.
68. Albanese, A.; Tang, P. S.; Chan, W. C., The effect of nanoparticle size, shape, and surface chemistry on biological systems. *Annu. Rev. Biomed. Eng.* **2012,** *14* (1), 1-16.

69. Hui, Y.; Yi, X.; Hou, F.; Wibowo, D.; Zhang, F.; Zhao, D.; Gao, H.; Zhao, C. X., Role of Nanoparticle Mechanical Properties in Cancer Drug Delivery. *ACS Nano* **2019,** *13* (7), 7410-7424.
70. Kapate, N.; Clegg, J. R.; Mitragotri, S., Non-spherical micro- and nanoparticles for drug delivery: Progress over 15 years. *Adv Drug Deliv Rev* **2021,** *177*, 113807.
71. Yamamoto, S.; Pietrasik, J.; Matyjaszewski, K., Temperature- and pH-responsive dense copolymer brushes prepared by ATRP. *Macromolecules* **2008,** *41* (19), 7013-7020.
72. Fouz, M. F.; Mukumoto, K.; Averick, S.; Molinar, O.; McCartney, B. M.; Matyjaszewski, K.; Armitage, B. A.; Das, S. R., Bright Fluorescent Nanotags from Bottlebrush Polymers with DNA-Tipped Bristles. *ACS Cent Sci* **2015,** *1* (8), 431-8.
73. Schneider, C. A.; Rasband, W. S.; Eliceiri, K. W., NIH Image to ImageJ: 25 years of image analysis. *Nat. Methods* **2012,** *9* (7), 671-5.
74. Rode Garcia, T.; Garcia Ac, A.; Lalloz, A.; Lacasse, F. X.; Hildgen, P.; Rabanel, J. M.; Banquy, X., Unified Scaling of the Structure and Loading of Nanoparticles Formed by Diffusion-Limited Coalescence. *Langmuir* **2018,** *34* (20), 5772-5780.
75. Frisken, B. J., Revisiting the method of cumulants for the analysis of dynamic light-scattering data. *Appl. Opt.* **2001,** *40* (24), 4087-91.
76. Safari, M. S.; Vorontsova, M. A.; Poling-Skutvik, R.; Vekilov, P. G.; Conrad, J. C., Differential dynamic microscopy of weakly scattering and polydisperse protein-rich clusters. *Phys. Rev. E Stat. Nonlin. Soft Matter Phys.* **2015,** *92* (4), 042712.
77. Rabanel, J. M.; Faivre, J.; Zaouter, C.; Patten, S. A.; Banquy, X.; Ramassamy, C., Nanoparticle shell structural cues drive in vitro transport properties, tissue distribution and brain accessibility in zebrafish. *Biomaterials* **2021,** *277*, 121085.
78. Wang, X.; Phan, D. T.; Sobrino, A.; George, S. C.; Hughes, C. C.; Lee, A. P., Engineering anastomosis between living capillary networks and endothelial cell-lined microfluidic channels. *Lab Chip* **2016,** *16* (2), 282-90.
79. Wang, X.; Phan, D. T. T.; Zhao, D.; George, S. C.; Hughes, C. C. W.; Lee, A. P., An on-chip microfluidic pressure regulator that facilitates reproducible loading of cells and hydrogels into microphysiological system platforms. *Lab Chip* **2016,** *16* (5), 868-876.
80. Jin, S. W.; Beis, D.; Mitchell, T.; Chen, J. N.; Stainier, D. Y., Cellular and molecular analyses of vascular tube and lumen formation in zebrafish. *Development* **2005,** *132* (23), 5199-209.
81. Kimmel, C. B.; Ballard, W. W.; Kimmel, S. R.; Ullmann, B.; Schilling, T. F., Stages of embryonic development of the zebrafish. *Dev. Dyn.* **1995,** *203* (3), 253-310.
82. Chen, Y.; Liang, Z.; Blanchard, J.; Dai, C. L.; Sun, S.; Lee, M. H.; Grundke-Iqbal, I.; Iqbal, K.; Liu, F.; Gong, C. X., A non-transgenic mouse model (icv-STZ mouse) of Alzheimer's disease: similarities to and differences from the transgenic model (3xTg-AD mouse). *Mol. Neurobiol.* **2013,** *47* (2), 711-25.
83. Franklin, K. B. J.; Paxinos, G., *The Mouse Brain in Stereotaxic Coordinates*. Academic Press: 1997.
84. Barbash, S.; Hanin, G.; Soreq, H., Stereotactic injection of microRNA-expressing lentiviruses to the mouse hippocampus ca1 region and assessment of the behavioral outcome. *J Vis Exp* **2013,** (76), e50170.